Automated Bridge Inspection using Digital Image Correlation Phase III: Examination Alternative Vision-based Methods and Deployment Mechanisms for Field Implementation

William Collins, PhD, PE
Assistant Professor
Department of Civil, Environmental &
Architectural Engineering
The University of Kansas

Caroline Bennett, PhD, PE
Professor

Jian Li, PhD, PE
Associate Professor

Mary Juno
Research Assistant

Hayder Al-Salih
Research Assistant

KU THE UNIVERSITY OF KANSAS

2023

University of Nebraska Lincoln
The University of Iowa
KU The University of Kansas
Missouri S&T
Lincoln University Missouri
Nebraska Indian Community College
University of Nebraska Omaha
University of Nebraska Medical Center
KU Medical Center The University of Kansas

Automated Bridge Inspection using Digital Image Correlation Part III: Examination Alternative
Vision-based Methods and Deployment Mechanisms for Field Implementation

William Collins, Ph.D., P.E.
Assistant Professor
CEAE Department
University of Kansas

Caroline Bennett, Ph.D., P.E.
Professor
CEAE Department
University of Kansas

Jian Li, Ph.D., P.E.
Associate Professor
CEAE Department
University of Kansas

Mary Juno
Research Assistant
CEAE Department
University of Kansas

Hayder Al-Salih
Research Assistant
CEAE Department
University of Kansas

A Report on Research Sponsored by

Mid-America Transportation Center

University of Nebraska–Lincoln

September 2023

TECHNICAL REPORT DOCUMENTATION PAGE

1. Report No. 25-1121-0005-151-3	2. Government Accession No.	3. Recipient's Catalog No.
4. Title and Subtitle Automated Bridge Inspection using Digital Image Correlation Part III: Examination Alternative Vision-based Methods and Deployment Mechanisms for Field Implementation		5. Report Date September 2023
		6. Performing Organization Code
7. Author(s) William Collins, Ph.D., Caroline Bennett, Ph.D., Jian Li, Ph.D., Mary Juno, and Hayder Al-Salih		8. Performing Organization Report No. 25-1121-0005-151-3
9. Performing Organization Name and Address University of Kansas 2150 Learned Hall, 1530 W. 15th St. Lawrence, KS 66049		10. Work Unit No.
		11. Contract or Grant No. 69A3551747107
12. Sponsoring Agency Name and Address Mid-America Transportation Center		13. Type of Report and Period Covered Final Report June 2020 – June 2023
		14. Sponsoring Agency Code MATC TRB RiP No. 91994-68

15. Supplementary Notes
Conducted in cooperation with the U.S. Department of Transportation, Federal Highway Administration.

16. Abstract
One of the main concerns for aging steel bridges in the United States is the initiation and propagation of distortion-induced fatigue cracks. Distortion-induced fatigue cracks account for most of the fatigue cracks in bridges. Despite recent studies proving that visual inspections consistently fail to identify realistically sized fatigue cracks, Departments of Transportation are forced to rely primarily on the use of visual inspections to locate and characterize fatigue cracking. Many detection methodologies have been examined for fatigue crack detection, but the methods are dependent on detection equipment that is physically attached to the bridge, such as sensor networks, which limits the flexibility of the methods for analyzing the multiple fatigue susceptible regions present on highway bridges. The development of an inspection technique that is not dependent on human visual inspection or physical attachments would have the potential to decrease the time and cost of performing inspections, as well as decrease the risk of injury to inspectors and increase reliability.

The ability of vision-based technologies to serve as an alternative to manual inspections of highway bridges is an area of active research. While many vision-based technologies have been proven to detect macro-indicators of damage, digital image correlation (DIC) has shown potential for detecting and characterizing fatigue cracks. Since DIC measurements have the ability to capture full-field displacements and surface strains, it is proven that developed DIC methodologies have the ability to identify and characterize both in-plane and out-of-plane fatigue cracks, allowing application to steel bridges exposed to differential girder displacement. This report summarizes the development of a crack-detection methodology using DIC and focuses on the impact of crack complexity on the developed methodology. Research indicates that DIC is successful at detecting complex branched distortion-induced fatigue cracks, but automation presents challenges.

17. Key Words Fatigue, cracking, bridge, steel, inspection, digital image correlation	18. Distribution Statement No restrictions. This document is available through the National Technical Information Service, Springfield, VA 22161.		
19. Security Classif. (of this report)	20. Security Classif. (of this page)	21. No. of Pages 80	22. Price

Form DOT F 1700.7 (8-72) Reproduction of completed page authorized

Table of Contents

List of Figures

List of Tables

Disclaimer

The contents of this report reflect the views of the authors, who are responsible for the facts and the accuracy of the information presented herein. This document is disseminated in the interest of information exchange. The report is funded, partially or entirely, by a grant from the U.S. Department of Transportation's University Transportation Centers Program. However, the U.S. Government assumes no liability for the contents or use thereof.

Abstract

One of the main concerns for aging steel bridges in the United States is the initiation and propagation of distortion-induced fatigue cracks. Distortion-induced fatigue cracks account for most of the fatigue cracks in bridges. Despite recent studies proving that visual inspections consistently fail to identify realistically sized fatigue cracks, Departments of Transportation are forced to rely primarily on the use of visual inspections to locate and characterize fatigue cracking. Many detection methodologies have been examined for fatigue crack detection, but the methods are dependent on detection equipment that is physically attached to the bridge, such as sensor networks, which limits the flexibility of the methods for analyzing the multiple fatigue susceptible regions present on highway bridges. The development of an inspection technique that is not dependent on human visual inspection or physical attachments would have the potential to decrease the time and cost of performing inspections, as well as decrease the risk of injury to inspectors and increase reliability.

The ability of vision-based technologies to serve as an alternative to manual inspections of highway bridges is an area of active research. While many vision-based technologies have been proven to detect macro-indicators of damage, digital image correlation (DIC) has shown potential for detecting and characterizing fatigue cracks. Since DIC measurements have the ability to capture full-field displacements and surface strains, it is proven that developed DIC methodologies have the ability to identify and characterize both in-plane and out-of-plane fatigue cracks, allowing application to steel bridges exposed to differential girder displacement. This report summarizes the development of a crack-detection methodology using DIC and focuses on the impact of crack complexity on the developed methodology. Research indicates that DIC is

successful at detecting complex branched distortion-induced fatigue cracks, but automation

presents challenges.

Chapter 1 Digital Image Correlation Background

1.1 Introduction

Bridges are vital to the movement of goods and people across the country but are prone to damage and deterioration from repetitive loads over their long service life. In their most recent Infrastructure Report Card, the American Society of Civil Engineers gave bridges in the United States a grade of C and found that over 7.5 percent of bridges are considered structurally deficient (ASCE 2021). Identifying and repairing potential issues is vital to properly maintaining bridges and ensuring that they remain in-service for at least the entirety of their intended service life.

One of the major issues impacting older steel bridges is the initiation and propagation of fatigue cracks (Fisher 1984), specifically distortion-induced fatigue cracks, which account for almost 90% of fatigue cracks in aging steel bridges in the United States (Connor and Fisher 2006). Steel bridges built prior to the 1980s in the United States were regularly designed without a connection between the flanges and connection plate, which can increase the rate of initiation for distortion-induced fatigue cracks (Zhao and Roddis 2004). When a bridge with this detail experiences traffic loads, the girders are subjected to differential deflection. The differential deflection can allow the cross-frame to push or pull on the girder web which causes out-of-plane stresses to be applied to the weak web gap region, resulting in distortion-induced fatigue cracks.

To minimize the potential impact of distortion-induced fatigue cracking, bridges are required to be repaired or retrofitted based on the findings of regular inspections. Bridge inspections are typically performed on a 24-month cycle (FHWA 2004), and the most common method for fatigue crack detection is through visual inspection. Fatigue cracks are caused by cyclic traffic loads, and they are initially very small and challenging to detect through visual

inspection. When cracks go undetected, however, they have the potential to propagate to a critical size, which could compromise a bridge's structural integrity. Although bridge inspections are necessary to ensure the safety of bridge infrastructure, visual inspections have significant monetary and time costs, as well as present safety risks to both inspectors and the travelling public. Additionally, the identification of realistic fatigue cracks has been proven to be extremely difficult and inconsistent (Campbell et al. 2020; Whitehead 2015; Zhao and Haldar 1996).

Technologies to detect and monitor cracking has been evaluated by researchers interested in structural health monitoring (SHM) and non-destructive testing (NDT). While sensing technologies have been used successfully to detect and monitor both in- and out-of-plane cracks, many of these approaches require the use of sensors or other components that physically attach to a particular location on a bridge, preventing these methodologies from effectively monitoring the various regions of fatigue susceptibility on steel bridges. The development of a computer vision-based detection methodology that would operate without depending on a physical attachment would allow large sections of steel bridges to be surveyed safely and efficiently.

Some research has been performed on vision-based crack detection methodologies, but the majority of testing conducted was under highly idealized conditions that only evaluated in-plane fatigue loading or non-metallic materials (Vanlanduit et al. 2009; Rupil et al. 2011; Nowell et al. 2010). Very few research programs have evaluated vision-based crack detection methods on out-of-plane fatigue loading or with the complex geometries commonly found on steel highway bridges. A vision-based crack detection methodology that utilizes digital image correlation (DIC) is being evaluated for performance on both ideal and non-ideal in-plane lab setups and out-of-plane test setups with complex geometry and distortion-induced fatigue cracking.

1.2 Digital Image Correlation Methodology

1.2.1 Computer Vision

       Computer vision refers to the branch of technology that utilizes computer algorithms and optics to collect information from pictures and videos. Researchers in engineering and material sciences have evaluated the use of computer vision for different applications, particularly to characterize mechanical parameters. The ability of computer vision to detect cracks has been evaluated by many researchers using a variety of materials. Edge detection methodologies have been proven to be able to successfully identify edge-like features on digital images, allowing for detection and localization of cracks in concrete surfaces (Abdel-Qader et al. 2003). Due to inadvertent detection of corrosion, surface textures, component boundaries, and defects, edge detection in metallic materials continues to have a high rate of false positives (Yeum and Dyke 2015).

       Research has been conducted to develop algorithms that could remove thick, short, or exceedingly linear edges that are typically not created by cracking, with the goal of creating a reliable crack detection methodology (Yu et al. 2007). Complex algorithms for detecting cracking in asphalt and concrete pavements have been developed by other researchers (Yamaguchi and Hashimoto 2010; Zou et al. 2012; Cha et al. 2017). Typically, asphalt and concrete pavements have larger crack openings than metallic materials, as well as higher contrast between cracked and uncracked regions, meaning that the application of edge detection methodologies to steel bridges is challenging. Additionally, most computer vision studies focus on macro-indicators of damage, such as extensive corrosion, concrete deck deterioration, and large displacements caused by substructure movement. A computer vision strategy to detect

fatigue cracks through the tracking of structural surface motion in a video has been developed, but crack tip identification remains a challenge (Kong and Li 2018).

1.2.2 Digital Image Correlation Background

DIC is a subset of computer vision that utilizes medium- to high-resolution cameras and post-processing computer software to analyze images and outputs full-field surface displacement. A three-dimensional strain field can be developed from the full-field surface displacement. DIC software is capable of analyzing both two- and three-dimensional data, depending on how many cameras are utilized during testing. DIC compares a series of images that are collected during loading and generates relative strain and displacement for each point on the image. DIC has been proven to have potential for detecting and characterizing fatigue cracks, but the majority of testing has been limited to simplified test setups, such as in-plane loading or simple geometry.

DIC has been used in the place of tradition sensing methods, such as strain gauges and extensometers, to determine both strain and deformation (Yuan et al. 2014). Crack detection using DIC has been applied to a concrete structure (Küntz et al. 2006) and in the calculation of stress intensity factors (Zhang and He 2012; Hamam et al. 2007). The applications and limitations of 3D DIC have been evaluated using simplified test setups since the mid-1990s (Helm 1996). Test setups with four cameras have been used to determine out-of-plane displacements, but additional cameras result in challenges with the experimental setup and calibration (Chen et al. 2013). A stereoscopic camera setup with a high shutter speed has been used to measure full-field out-of-plane vibrations, but the use of high-speed cameras resulted in a lack of image resolution (Helfrick et al. 2011). Some complex loading scenarios have been tested using clevis fixtures to generate mixed mode loading on compact (C(T)) test specimens. For

Mode I (opening) and Mode II (in-plane shear) loading, DIC displacement results agreed with results developed using a finite element analysis of the crack (Sutton et al. 2007).

DIC has been used to evaluate in-plane displacements for a variety of civil infrastructure. A primary application of DIC is to measure deflections of critical bridge members when subjected to service loading. Bridge deflection has been measured from digital videos through a combination of DIC and an inverse compositional algorithm (Pan et al. 2016). This methodology was validated by testing an in-service railway bridge. An advanced DIC system was used to investigate the deflections of two historic masonry arch bridges under service loads (Dhanasekar et al. 2018). Similar work was performed by Cigada et al. (2014) and Alipour et al. (2019). 3D-DIC has also been used with an unmanned aerial vehicle to examine surface cracking on a concrete bridge (Reagan et al. 2018). While there have been successful applications of DIC for evaluating deflections of in-service structures, challenges to field deployment have been identified, particularly lighting conditions (Ribeiro et al. 2014) and limitations on how large of a distance there is between the camera and the material surface (Lee and Shinozuka 2006).

Extensive research has been performed on applications of DIC for identifying fatigue cracks in metallic materials, but the research has primarily been conducted in an idealized laboratory setting. Studies have examined in-plane fatigue cracking with the goal of identifying and characterizing cracks. In-plane loading studies have been performed on steel C(T) specimens (Rupil et al. 2011), aluminum channels (Vanlanduit et al. 2008), notched tension specimens (Carrol et al. 2009; Carrol et al. 2012), and tension plates with center drilled bolt holes (Lorenzino et al. 2014; Hutt and Cawley 2009). These studies have contributed to understanding the limitations and abilities of DIC for crack detection. Most of these studies, however, focus on qualitative crack identification and characterization, and the development of a

quantifiable methodology for automated steel bridge inspections has only been minimally investigated. Additionally, out-of-plane loading conditions have not been as thoroughly researched as in-plane fatigue loading. This is likely due to the complexity of the test setup required for out-of-plane fatigue loading (Sutton et al. 2007). Work was performed to begin to evaluate how DIC works for complex, out-of-plane test setups, and initial testing found that the developed methodology had the ability to detect and predict the length of distortion-induced fatigue cracks (Dellenbaugh et al. 2020).

1.2.3 Digital Image Correlation Setup

In theory, accurate DIC results are dependent on the specimen preparation, camera setup, calibration, and image collection. The preparation of the specimen primarily refers to the application of a speckle pattern. The ideal pattern is made of consistent dot sizes that are high contrast and random. The speckle pattern is what provides points of reference for the DIC software. Without a speckle pattern, images cannot be compared to evaluate the movement of the specimen. The camera setup depends on the test specimen's complexity and whether two- or three- dimensional analysis is desired. For two-dimensional analysis, one camera will suffice, since no out-of-plane deformations are expected, which allows for a simplified test setup and easier calibration. When testing for out-of-plane displacements, two or more cameras are needed to capture the three-dimensional strain field. Calibration is the process of converting the images from pixels to real dimensions, ensuring realistic evaluation of the specimen. Additionally, calibration accounts for the location of the cameras relative to one another in test setups with two or more cameras. After calibrating, images are collected at a constant interval while the test specimen is being loaded. These images are analyzed using DIC software to determine full-field displacements and stresses.

Chapter 2 Previous Work Overview

2.1 Initial In-Plane Testing

2.1.1 Initial Testing and Methodology Development

To develop an automated fatigue crack inspection methodology, a method for quantifying cracking was needed. The initial methodology was developed using a DIC test setup with a single camera and a C(T) specimen subjected to in-plane loading in a servo-hydraulic testing machine. The C(T) specimen tested was 6.35 mm (0.25 in.) thick and 127 mm (5.0 in.) wide. The specimen size was chosen such that a single specimen could accommodate extensive crack growth and testing at multiple crack lengths. Since bridges are subjected to highly variable loadings, multiple load cases were defined for testing on the C(T) specimen. Stress intensity ranges of 11, 22, 33, 44, and 55 MPa√m (10, 20, 30, 40, and 50 ksi√in) were chosen to emulate realistic bridge loading, and the stress intensity ranges were tested from lowest to highest to limit crack tip plasticity during testing. Images for DIC processing were collected for each loading case at crack lengths of 12.7, 25.4, 38.1, and 50.8 mm (0.5, 1.0, 1.5, and 2.0 in.). The general location of the crack was identifiable through visual inspection of the DIC results, but a methodology to determine the crack length from the DIC data was developed to move towards automation. The twenty data sets for in-plane testing were used to develop a crack length quantification methodology.

2.1.2 Crack Characterization Methodology

Original testing was performed on a C(T) specimen to ensure that the crack location was easily identified. Using the known crack path, the coordinates of the crack path were extended beyond the crack tip, assuming that crack growth would continue linearly. After identifying the crack path, inspection lines were plotted orthogonal to the crack path at consistent intervals along

the crack path and projected crack path. From each orthogonal inspection line, two hundred data points were extracted to determine the relative displacement between the two sides of the crack. The difference between the displacement on either side of the crack was defined as the relative displacement. Relative displacements were plotted along the length of the crack path, and the best fit line for each side of the crack was determined using an algorithm. The relative displacement for each point along the crack path, Δ_i, was divided by the maximum relative displacement for the data set, Δ_{max}. Convergence of the crack was defined as the difference between 100% and the ratio of relative to maximum displacement, shown below as

$$Convergence = 100\% - \frac{\Delta_i}{\Delta_{max}}. \tag{2.1}$$

Theoretically, convergence should equal 100% at the crack tip as there is no relative displacement on either side of the crack, while at the crack opening where relative displacement is the greatest, compliance should equal 0%. However, initial results indicated this was rarely true, likely due to non-ideal testing conditions, such as speckle pattern and image resolution. Initial testing showed that the crack tip was located at a convergence between 90% and 95%. This was then tested in an out-of-plane test setup to determine the accuracy and efficacy of the developed methodology.

2.2 In-Plane Lighting and Focus Testing

2.2.1 Lighting and Focus Background

The accuracy of DIC output is dependent on the preparation of the specimen, camera setup, calibration, and image collection. Work performed during year one was primarily proof-of-concept and was applied under idealized conditions. For DIC to be implementable in the field,

the system and methodology needs to be robust enough to handle the varying conditions found

on in-service structures. The objective of this study was to evaluate the ability of the developed

DIC methodology to characterize an in-plane crack under non-idealized lighting and camera

focus conditions.

2.2.2 Lighting and Focus Testing Test Setup, Loading, and Conditions

Light and focus testing was performed on steel C(T) specimens loaded in a uniaxial

servo-hydraulic loading frame, similar to the testing that developed the in-plane methodology.

The fatigue crack investigated had the same four crack lengths used in the initial testing, but

loading was redefined to achieve stress intensity ranges of 11, 16, 22, 27, and 33 MPa$\sqrt{m}$ (10,

15, 20, 25, and 30 ksi$\sqrt{in}$). These load cases are respectively designated LC1 through LC5. The

five load cases were modified from year one testing to limit plasticity at the crack tip and to

provide a more realistic loading range.

Three lighting conditions and three focus conditions were defined. High light was the

brightest, achieved when two external LED lamps were set to the maximum brightness, which

created an overexposed image with a washed-out speckle pattern. Medium light and low light

were approximately 70% and 30% of the high light condition, respectively. Ideal lighting would

occur at approximately 85% of the high light condition, meaning that all lighting conditions were

non-ideal, based on a range of lumens for each lighting condition.

The crack characterization methodology was developed for a camera distance of 216 mm

(8.5 in.). Two additional camera distances, 432 and 648 mm (17.0 and 25.5 in.), were evaluated

in this study. At each of the three camera distances, the ideal focus and two additional levels of

focus resulting in a 5% and 10% reduction from the ideal focus, respectively, were chosen for

testing. Using the uncertainty estimate from the DIC software, ideal focus was defined as having

an uncertainty of 0.0003 mm (0.00001 in.) or better under the high lighting condition. Focus initially varied by manually adjusting the rotation of the camera's focus ring. However, the focus ring used does not measure rotation, therefore an alternative definition for quantifying focus was developed. Focus was redefined in terms of camera distance from the specimen. By first focusing the camera at the ideal distances of 216, 432, and 648 mm (8.5, 17.0, and 25.5 in.), the camera was then moved closer to the specimen, reducing the focal length by 5% and 10% to create the fair and poor focus conditions, respectively. The uncertainty estimates for the fair and poor focus conditions were 0.0007 and 0.0010 mm (0.00003 and 0.00004 in.), respectively.

Six combinations of lighting and focus conditions were evaluated for each of the three camera distances for in-plane crack lengths of 12.7, 25.4, 38.1, and 50.8 mm (0.5, 1.0, 1.5, and 2.0 in.). Appendix A details all the testing conditions defined for each camera to specimen distance. All six testing condition combinations evaluated were sub-optimal, ignoring the recommended calibration needs of the DIC system.

2.2.3 Lighting and Focus Testing Results

DIC data was collected for varying crack lengths and lighting and focus conditions. Typical outputs from the DIC software for LC5 with a crack length of 25.4 mm (1.0 in.) and a camera-to-specimen distance of 648 mm (25.5 in.) are shown in Figures 2.1 and 2.2, showing conditions 1 and 5, respectively.
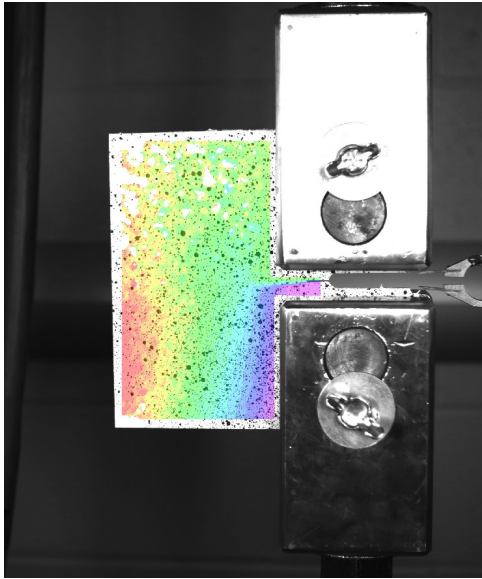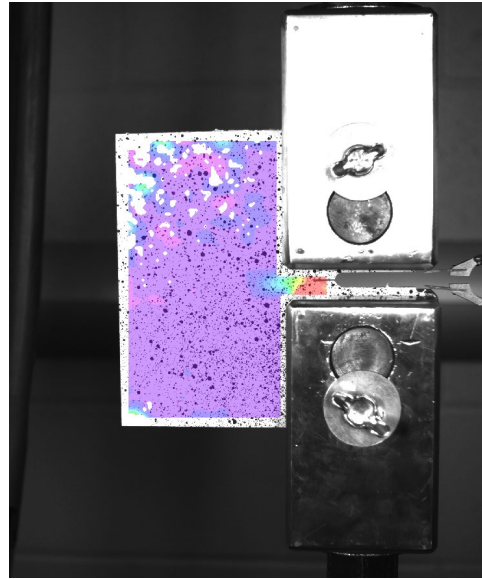
(a)   (b)

Figure 2.1 DIC results for a 25.4 mm (1.0 in.) crack with 648 mm (25.5 in.) camera distance under LC5 and Condition 1 in terms of (a) displacement and (b) strain
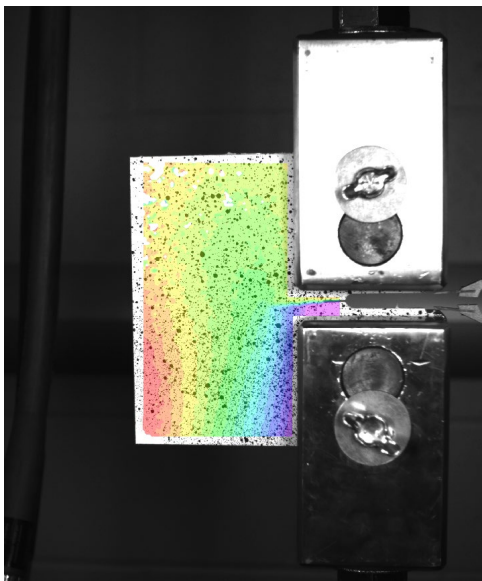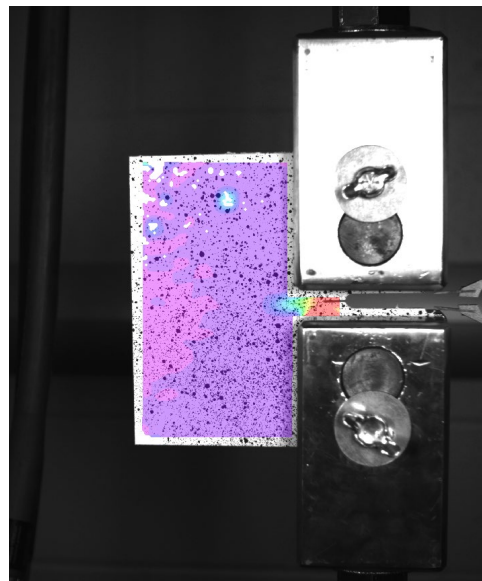
(a)   (b)

Figure 2.2 DIC results for a 25.4 mm (1.0 in.) crack with 648 mm (25.5 in.) camera distance under LC5 and Condition 1 in terms of (a) displacement and (b) strain

The expected deflections for C(T) specimens are exclusively in-plane, so relative displacements perpendicular to the crack path were utilized in accordance with the developed crack characterization methodology to calculate the convergence. Due to the distance between the camera and the specimen, the crack was not clearly visible in the DIC strain and displacement data images. Representative relative displacement and convergence values are shown in Figures 2.3 and 2.4 for LC5. In each plot, the vertical dotted line represents the actual crack length, as verified through specimen compliance and visual observation. Relative displacement and convergence plots for additional crack lengths, load cases, and camera distances are shown in Appendix A. The high, medium, and low light conditions are denoted using HL, ML, and LL, respectively, while the ideal, fair, and poor focus conditions are denoted by IF, FF, and PF, respectively. Thus, the first condition combining high light and ideal focus is termed HLIF.
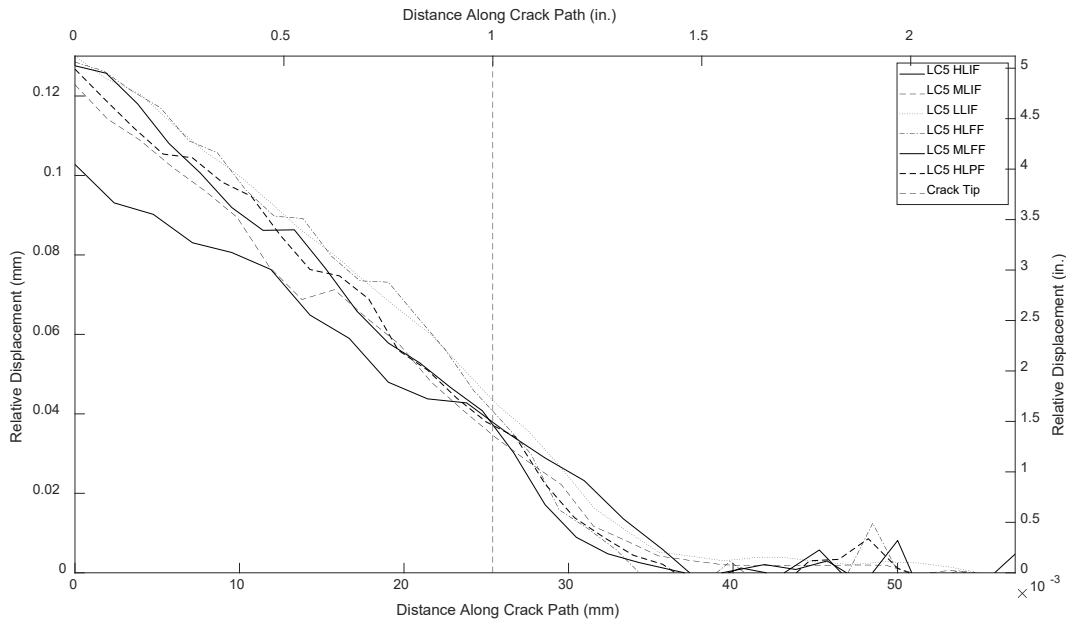
Figure 2.3 Relative displacement of a 25.4 mm (1.0 in.) crack under LC5
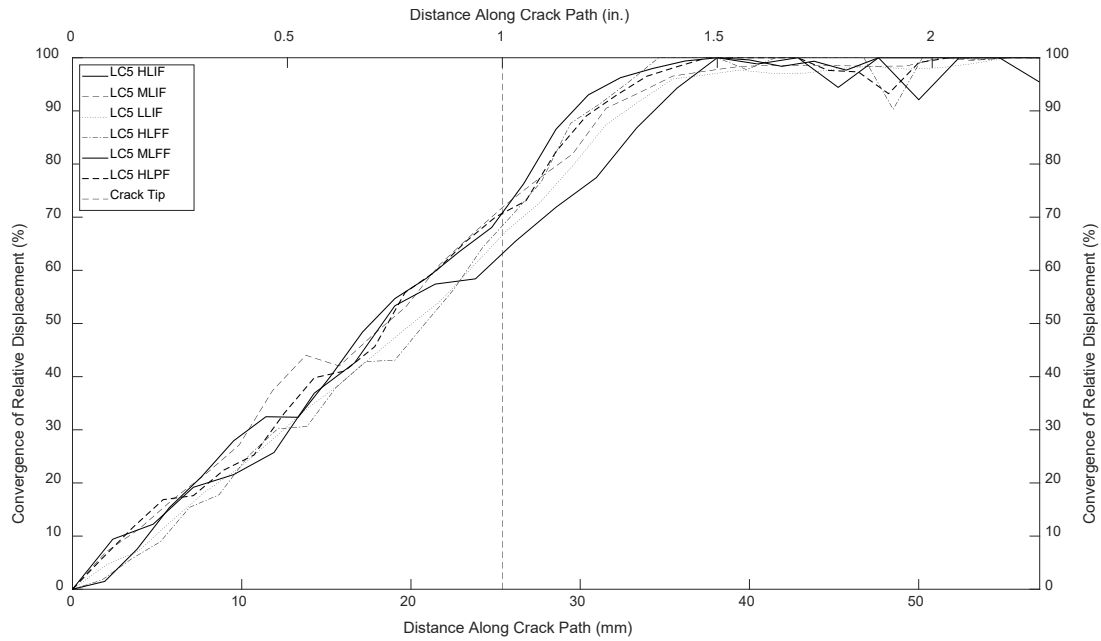
Figure 2.4 Convergence of relative displacement of a 25.4 mm (1.0 in.) crack under LC5

Convergence values for each lighting and focus condition combination were averaged across all five load cases for a crack length of 25.4 mm (1.0 in.) and camera distance of 648 mm (25.5 in.) and are compared to the ideal case in Table 2.1. The convergence for each condition and load case is shown visually in Figure 2.5. Because of the modified loading cases from the initial methodology development, the non-ideal cases can only be directly compared with the ideal results for load cases 1, 3, and 5. The lines are presented for clarity.

Table 2.1 Average convergence at 25.4 mm (1.0 in.) crack tip for 648 mm (25.5 in.) camera distance

Light and Focus Condition	Average Convergence	Difference
Ideal	92.6%	N/A
1	71.5%	21.1%
2	72.3%	20.3%
3	69.6%	23.0%
4	73.3%	19.3%
5	66.2%	26.4%
6	73.1%	19.5%
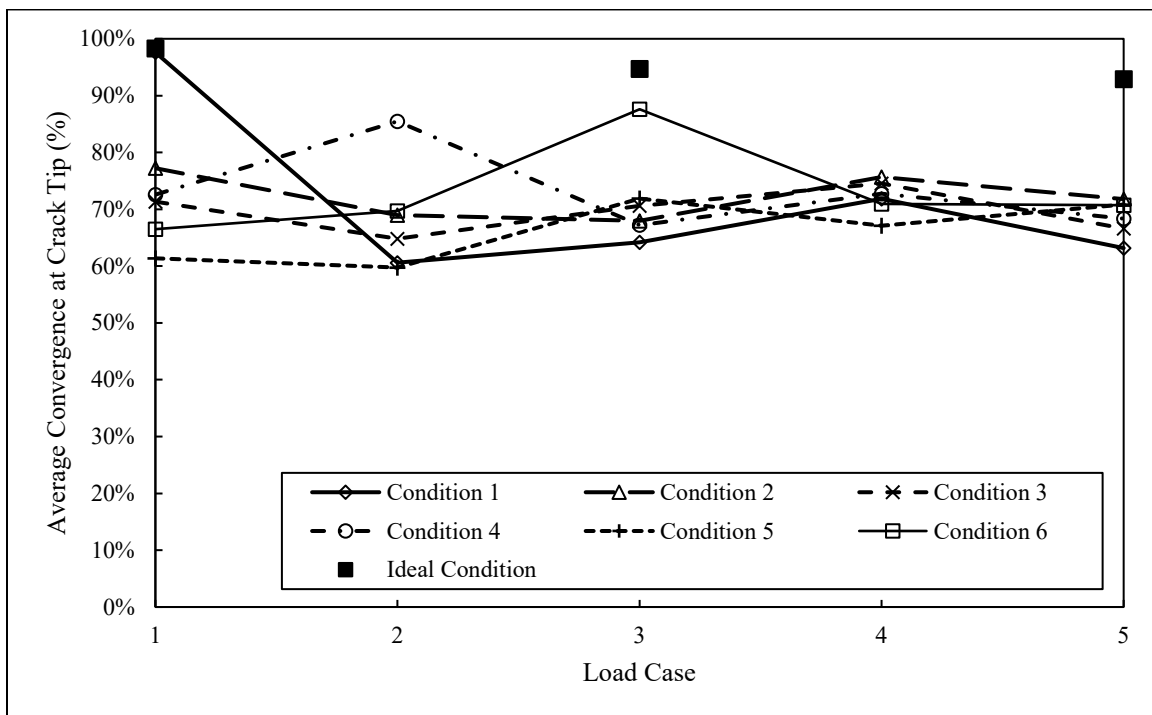
Figure 2.5 Average convergence at crack tip for each load case and condition for a crack of 25.4 mm (1.0 in.) with a camera to specimen spacing of 648 mm (25.5 in.)

Convergence values for non-ideal conditions exhibit significant variability compared to the results from the ideal test conditions. While the non-ideal conditions resulted in a significant decrease in crack convergence and DIC output quality, the presence of a crack was still detected.

This indicates that sub-optimal conditions may not result in accurate crack length measurements, but can be used to detect cracks and flag them for further inspection. Similar results were seen for all crack lengths and camera to specimen distances. Additional information on lighting and focus condition testing can be found in Juno (2020).

2.3 Study on the Impact of Aperture

2.3.1 Aperture Background

Aperture is a measure of how open the lens of a camera is. This is the component that controls the physical amount of light allowed into the camera. Aperture is defined based on the "f-stop" number, where f/1.4 allows a large amount of light into the camera and f/11 or higher lets a very small amount of light in. Figure 2.6 shows a comparison between different aperture values on a C(T) specimen with a camera to specimen distance of 305 mm (12.0 in.). All photographs were taken with the same external lighting conditions, from the same location, and have no post-processing or editing.

(a)   (b)   (c)
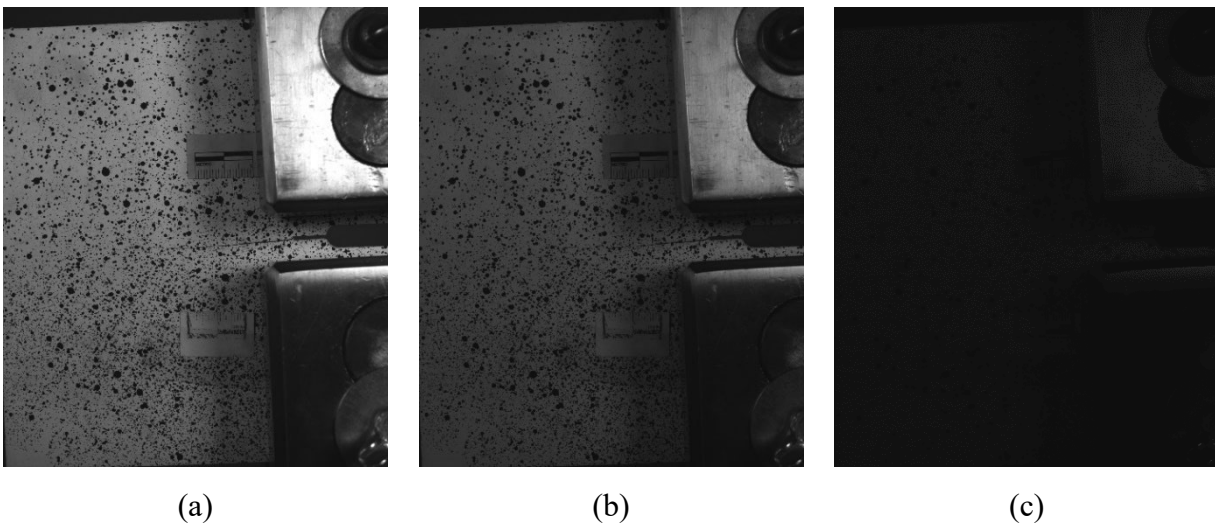
Figure 2.6 C(T) specimen photographed with apertures of (a) f/2.8; (b) f/4; and (c) f/11

Aperture also has some impact on the camera field depth. The larger the camera opening is, the smaller the field depth, and the closer the camera would need to be to the specimen. Some cameras have lenses that can automatically adjust aperture, but the cameras utilized in this study must be changed manually, making understanding the impact of the aperture on DIC results important.

2.3.2 Aperture Testing Setup and Loading

Testing for the impact of aperture was performed on the same C(T) specimen after the conclusion of the lighting and focus study, so it was performed on a single crack length of 50.8 mm (2.0 in.) under LC5. Images were collected for four different camera-to-specimen distances and for four different aperture values with idealized light and focus conditions. The four camera-to-specimen distances were 203, 305, 457, and 610 mm (8.0, 12.0, 18.0, and 24.0 in.). Data was collected for apertures of f/1.4, f/2.8, f/4, and f/11, but due to low light and poor quality of the f/4 and f/11 images, only images taken with apertures of f/1.4 and f/2.8 were analyzed using DIC.

2.3.3 Aperture Study Results

A convergence plot for the 50.8 mm (2.0 in.) crack with a camera distance of 203 mm (8.0 in.) and an aperture of f/1.4 is shown in Figure 2.7. The camera distance and aperture setting almost exactly match the initial testing performed on the C(T) specimen, and results in a similar convergence seen in previous testing. This convergence plot is representative of the remaining seven combinations of camera distance and aperture, which are presented in Appendix A. Convergence plots for the other conditions displayed more noise near the middle of the crack, but the amount of noise did not seem to vary with aperture setting or camera distance. The aperture of f/2.8 resulted in higher convergence values for all camera distances except for 305 mm (12.0 in.) as shown in Table 2.2.
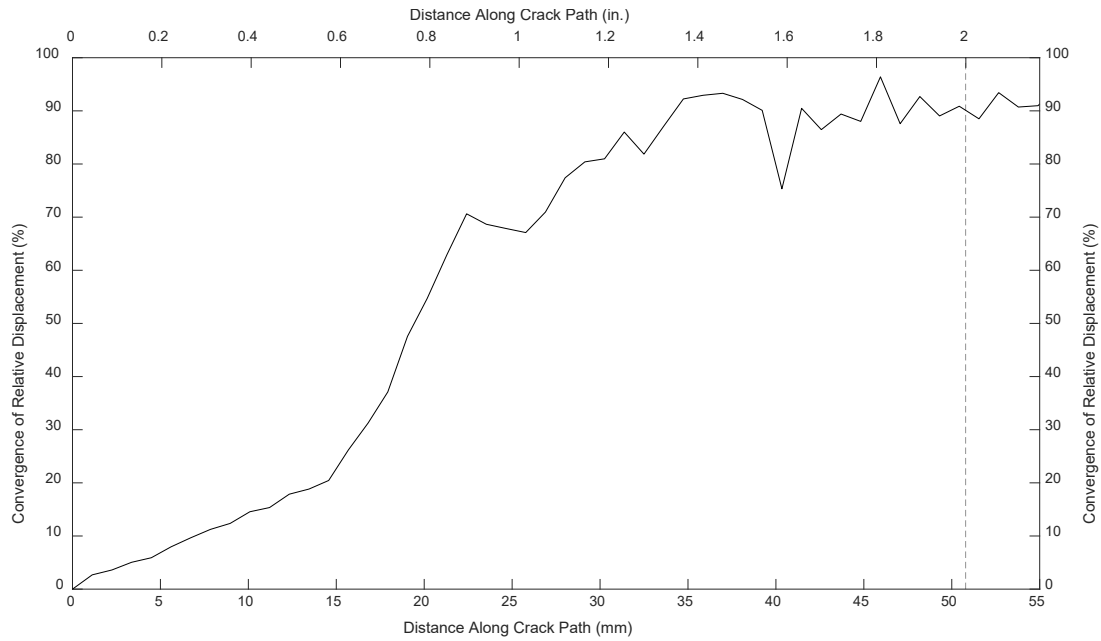
Figure 2.7 Convergence of relative displacement of a 50.8 mm (2.0 in.) crack with a camera distance of 203 mm (8.0 in.) and an aperture of f/1.4 under LC5

Table 2.2 Convergence of 50.8 mm (2.0 in.) crack under varying camera distances and aperture conditions

Camera to Specimen Distance, mm (in.)	Aperture Setting	
	f/1.4	f/2.8
203 (8.0)	90.1%	95.0%
305 (12.0)	84.9%	78.1%
457 (18.0)	74.7%	87.4%
610 (24.0)	79.3%	82.9%
Avg.	82.3%	85.9%

Aperture could potentially serve to correct for non-ideal lighting and focus conditions. Additional research will need to be performed to evaluate exactly how much aperture impacts the quality of image focus. Other than this brief investigation, all testing has been performed with an aperture of f/1.4, which is the largest aperture possible on the cameras used for testing. Using a

camera with an automatic focusing lens and an adjustable aperture could help to simplify the test setup required on a UAV and result in higher quality images.

2.4 Initial Distortion-Induced Fatigue Testing

2.4.1 Distortion-Induced Fatigue Test Setup and Loading

After the crack characterization methodology was developed using a simplified in-plane C(T) specimen, the methodology was evaluated on a crack developed on a half-scale girder-to-cross-frame subassembly. The test specimen was an I-shaped plate girder sub-assembly fabricated from A36 steel. The half-scale girder had a length of 2845 mm (112 in.), a depth of 917 mm (36.1 in.), and a web thickness of 10 mm (0.375 in.). To approximate the axial stiffness provided by the concrete deck attached to the top flange of a girder, the top of the girder sub-assembly was connected to the reaction floor of the laboratory, which prevented the top flange from experiencing out-of-plane motion. A cross-frame was installed at the mid-span of the girder, which was attached through a connection plate welded only to the girder web.

The girder was loaded out-of-plane by applying a vertical displacement to the far end of the cross-frame, producing a distortion-induced fatigue crack. Fatigue cracking was initiated in the web-gap region between the connection plate and the flange. A fatigue crack was initiated and propagated on the girder through loading for 21,000 cycles at a load range of 2.2 to 25.5 kN (0.5 to 5.75 kips). This crack spanned between the connection plate weld and the girder web and contained two vertical segments connected by a short diagonal segment, all of which were idealized as linear. The crack was measured to have a total length of 44.5 mm (1.75 in.).

A loading protocol was developed for the out-of-plane testing to have varying and realistic loads that simulate the varying traffic loads that bridges are subjected to. Realistic loading levels were determined using a finite element model of a bridge based on the full-scale

proportions of the testing setup. Realistic differential vertical deflections between adjacent girders were determined by applying the AASHTO fatigue truck. On the full-scale finite element model, the differential deflection was 2.54 mm (0.1 in.), so the target differential deflection for the half-scale test setup was 1.25 mm (0.05 in.), which corresponds to an actuator load of 6.6 kN (1.5 kips) applied to the end of the cross-frame. Seven load cases were defined for loads above and below the target load. All loading cases had a minimum applied load of 0.89 kN (0.2 kip) to simulate the dead load of the bridge, and the load cases had a maximum applied load of 2.2, 4.4, 6.7, 8.9, 11.1, 13.3, and 15.6 kN (0.5, 1.0, 1.5, 2.0, 2.5, 3.0, and 3.5 kips).

2.4.2 Distortion-Induced Fatigue DIC Configuration

The main difference between the DIC configuration for in-plane C(T) testing and distortion-induced fatigue testing is that out-of-plane testing requires the use of a two-camera stereo setup, rather than a single camera (see fig. 2.6a and b). A speckle pattern was applied to the fatigue susceptible region to provide reference points for the DIC processing (see fig. 2.6c). For the purpose of processing the DIC data, the web-to-flange weld was defined as the x-axis, the stiffener-to-web weld was established as the y-axis, and the z-axis was located along the direction of the cross-frame.
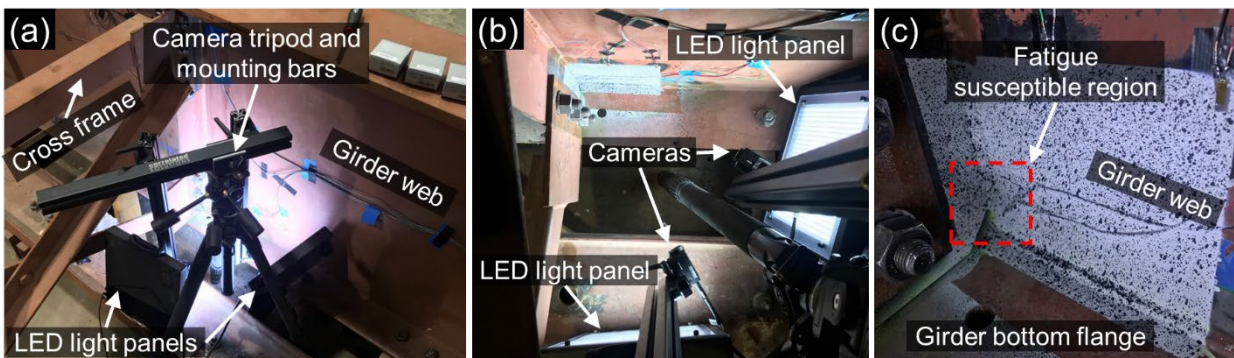
Figure 2.8 (a) Hardware locations for out-of-plane testing, (b) hardware orientation as seen from above, and (c) fatigue susceptible region with speckle pattern applied

2.4.3 Distortion-Induced Fatigue Crack Characterization Methodology

The same methodology was used to analyze distortion-induced fatigue specimens as the in-plane specimens. For the initial analysis of distortion-induced fatigue cracks, the displacement values along the z-axis were used to determine convergence. Despite the more complicated geometry, the crack path could be determined through visual inspection of the DIC displacement contours. Orthogonal lines were drawn along the length of the crack in the web gap region. The relative displacements were determined for the entire length of the crack and extended beyond the crack tip. Convergence was calculated for the out-of-plane cracking in the same manner as the in-plane crack using equation 2.1.

The relative displacements for the load case ranging from 0.89 to 2.2 kN (0.2 to 0.5 kip) were very small for the entirety of the crack length, which resulted in large variations in convergence. The high variability of the convergence indicates that the developed methodology is not applicable at low load levels. This applicability threshold will need to be investigated further in future testing.

Because the C(T) specimen testing resulted in typical convergences of 90% to 95%, the known crack length for the distortion-induced fatigue specimen was compared to the 90% and 95% convergence values to determine the accuracy of the developed DIC results. The optically measured crack length was 44.5 mm (1.75 in.). The 90% convergence values tended to under-predict the crack length. On average, the 90% convergence value corresponded to a 40.6 mm (1.59 in.) crack, which is 9% lower than the actual crack. The 95% convergence tended to over-predict the crack length, but only by an average of 1%, corresponding to a predicted crack length of 45.0 mm (1.77 in.). This indicated that the developed methodology for crack length determination was accurate for simple out-of-plane cracks.

2.5 Investigation into Open-Source DIC Alternatives

2.5.1 Open-Source Software Overview

Open-source software has the potential to allow for more flexible analysis of DIC data. Additionally, open-source software could allow for different data collection methods, without the need for specialized, idealized test setups. This is important for the development of an accessible inspection system. In this study, three viable open-source alternatives were identified and assessed using the existing data sets.

2.5.2 Open-Source Software Alternatives

The International DIC Society (2018) has identified several open-source programs that have been developed by the research community and made available to fellow researchers. Of the options presented, three emerged as potentially viable alternatives for use in automated bridge inspections: *Ncorr*, Augmented Lagrangian DIC (*ALDIC*), and DICengine (*DICe*). There were additional options that were feasible for analyzing fatigue cracks on steel bridge members, but only these three alternatives were investigated deeper due to incompatible operating systems, lack of knowledge of the software language, or lack of software documentation. These three open-source alternatives were used to analyze both in- and out-of-plane cracks using images obtained during the development of the crack characterization methodology. The results obtained from these open-source software packages are shown in Appendix A.

Ncorr is a 2D DIC program developed by the Georgia Institute of Technology in Georgia, United States (Blaber et al. 2015). Designed to address a lack of user-friendly alternatives, *Ncorr* is written entirely in MATLAB and features a high-quality graphical user interface (GUI). It introduces a Eulerian to Lagrangian conversion to analyze areas of discontinuities in displacement fields. When discontinuities are detected, the software creates a

region of interest and performs DIC on that area. Interpolation and a nonlinear optimization algorithm then determine the best fit for the areas with missing data. This has the potential to prove useful in images with poor focus or lighting conditions or with gaps in data due to non-ideal speckle pattern application. The built in user interface also includes contour plotting tools for visualizing the data quickly.

Developed by the California Institute of Technology in California, United States, *ALDIC* is a 2D DIC code also written in MATLAB (Yang and Bhattacharya 2020). It combines the speed and non-iterative analysis of local DIC and the displacement compatibility and smoothness of global DIC approaches. *ALDIC* utilizes subsets locally to determine multiple smaller displacement fields and then applies a compatibility requirement for global analysis to ensure there are no gaps or discontinuities in the displacement field without drastically increasing computation time.

DICe is a 2D and 3D DIC alternative written in C++ developed by the Sandia National Laboratories in New Mexico, United States (Turner 2015). It allows the user to choose between local and global DIC analysis methods and can also be applied in the tracking of rigid body motion. Like *Ncorr*, it is presented with an intuitive GUI, but does not feature the easy to use contour plotting options. Instead, output strain and displacement fields must be visualized using separate software or a free open-source data visualization application such as ParaView.

Chapter 3 Extended Complex Branched Distortion-Induced Fatigue Crack Testing

3.1 Complex Branched Distortion-Induced Fatigue Crack Test Setup and Loading

3.1.1 Complex Branched Crack Background

An important constraint for applications to DIC is the crack complexity capable of being analyzed. Testing was performed using the same test setup as the simple distortion-induced fatigue crack that was used for initial verification of the developed methodology (see fig. 2.6). For DIC to be implemented in the field, the methodology must be adequate for detection of any distortion-induced fatigue crack found on in-service structures. DIC was evaluated for its ability to quantify a complex, branched, distortion-induced fatigue crack.

3.1.2 Complex Branched Crack Test Setup

The out-of-plane distortion-induced fatigue testing was performed on the same half-scale girder-to-cross-frame subassembly as the initial out-of-plane loading testing. The test setup had a length of 2,845 mm (112 in.), a depth of 917 mm (36.1 in.), and a web thickness of 10 mm (0.375 in.). The bottom flange of the girder was restrained from motion through a connection to the strong floor of the laboratory, simulating the restraint provided by the concrete deck of a bridge. A cross-frame was attached by a welded connection plate to the center of the girder. The connection plate was only welded to the girder web, and since no connection was provided between the connection plate and the flanges of the girder, a fatigue-susceptible web-gap region was formed, shown in Figure 3.1. Differential girder displacement was simulated by applying a vertical load to the end of the cross-frame with a servo-hydraulic actuator, causing a distortion-induced fatigue crack to develop in the web-gap region. Additional details about the distortion-induced fatigue test frames can be found in Al-Salih et al. (2019) and Dellenbaugh et al. (2020).

Figure 3.1 Girder subassembly showing the web-gap region

3.1.3 Complex Branched Crack Pattern

To develop a complex, branched crack, the girder was loaded cyclically at a load range of

2.2 to 25.5 kN (0.5 to 5.75 kip) for approximately 1,700,000 cycles (Al-Salih et al. 2021). During

cyclic loading, two fatigue cracks propagated in the web-gap region; vertically along the

connection plate-to-web weld and horizontally along the web-to-flange weld. The vertical crack

along the connection plate-to-web weld also branched into the web in two locations. The overall

crack pattern is shown in Figure 3.2(a) with white lines drawn over the fatigue crack locations

for clarity. For evaluation, the bifurcated cracks were evaluated as three separate cracks. Each of

the four crack designations, paths, and lengths are summarized in Table 3.1.

<div align="center">(a)   (b)</div>
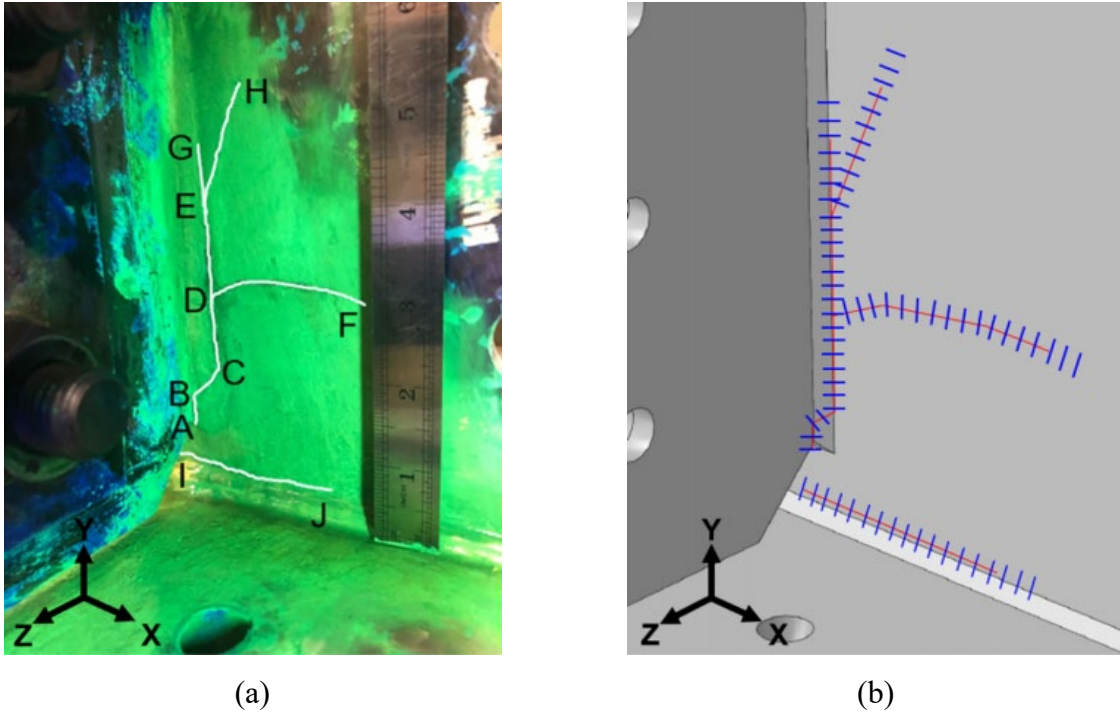
Figure 3.2 (a) Fatigue cracks in web-gap region and (b) schematic of crack path
with orthogonal data extraction lines

Table 3.1 Crack designations and lengths

Crack Name	Crack Path	Crack Length, mm (in.)
Vertical Crack	A-B-C-D-E-G	104.9 (4.14)
Branched Crack I	A-B-C-D-F	111.9 (4.41)
Branched Crack II	A-B-C-D-E-H	138.6 (5.45)
Horizontal Crack	I-J	51.0 (2.00)

3.1.4 Complex Branched Crack Data Collection Loading

A loading protocol had to be developed to achieve realistic loads for out-of-plane testing.

To this end, a finite element model of a full-scale bridge that matched the half-scale girder

proportions was developed. The bridge was loaded with the AASHTO fatigue truck and the

differential vertical deflections between adjacent girders were determined. For the full-scale

model, the differential deflection was 2.6 mm (0.102 in.), meaning that the target deflection for

the half-scale model was 1.3 mm (0.051 in.). To achieve the desired deflection, an actuator load

of 7.8 kN (1.75 kips) was applied (Dellenbaugh et al. 2019). Eleven load cases (LC) for DIC data

collection were defined with maximum loads above and below the target load, ranging from 2.2

to 24.5 kN (0.5 to 5.5 kips). The range in maximum load represented the variable loads bridges

are subjected to. For each load case, a minimum load of 0.9 kN (0.2 kip) was applied to simulate

the dead load acting on the bridge. The load and displacement ranges for each of the eleven load

cases is shown in Table 3.2.

Table 3.2 Out-of-plane load cases

Load Case	Load Range, kN (kips)	Displacement Range, mm (in.)
LC1	0.9 – 2.2 (0.2 – 0.5)	0.025 – 0.046 (0.001 – 0.002)
LC2	0.9 – 4.4 (0.2 – 1.0)	0.025 – 0.074 (0.001 – 0.003)
LC3	0.9 – 6.7 (0.2 – 1.5)	0.025 – 0.965 (0.001 – 0.038)
LC4	0.9 – 8.9 (0.2 – 2.0)	0.025 – 1.651 (0.001 – 0.065)
LC5	0.9 – 11.1 (0.2 – 2.5)	0.025 – 2.464 (0.001 – 0.097)
LC6	0.9 – 13.3 (0.2 – 3.0)	0.025 – 3.302 (0.001 – 0.130)
LC7	0.9 – 15.6 (0.2 – 3.5)	0.025 – 4.141 (0.001 – 0.163)
LC8	0.9 – 17.8 (0.2 – 4.0)	0.025 – 4.902 (0.001 – 0.193)
LC9	0.9 – 20.0 (0.2 – 4.5)	0.025 – 5.741 (0.001 – 0.226)
LC10	0.9 – 22.2 (0.2 – 5.0)	0.025 – 6.553 (0.001 – 0.258)
LC11	0.9 – 24.5 (0.2 – 5.5)	0.025 – 7.315 (0.001 – 0.288)

3.2 Complex Branched Distortion-Induced Fatigue Crack Characterization Methodology

3.2.1 Crack Characterization Methodology

The crack characterization methodology used to analyze the complex, multi-segment

distortion-induced fatigue crack was similar to the developed methodology used on the in-plane

testing and the simple out-of-plane crack methodology. DIC images were analyzed using

coordinate transformation. The *x*-axis was defined as parallel to the web-to-flange weld, the *y*-

axis follows the connection plate-to-web weld, and the *z*-axis is in the direction of the cross-frame, shown in Figure 3.2. Displacements in all three directions were analyzed due to the complex geometry of the test setup and the crack. Representative DIC results for each of the three displacements are shown in Figure 3.3.

(a) (b) (c)
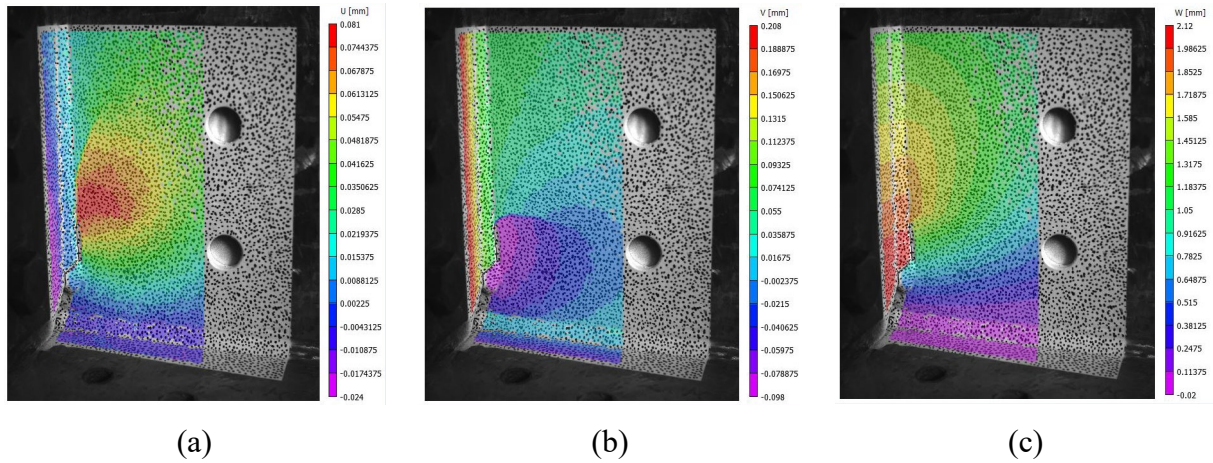
Figure 3.3 Representative DIC results for (a) U-displacement along the *x*-axis, (b) V-displacement along the *y*-axis, and (c) W-displacement along the *z*-axis

Due to the complexity of the crack, edge detection algorithms were not able to clearly detect the path of the crack. The crack paths were visually identified using dye penetrant in the loaded condition. The raw displacement data was then analyzed following the developed methodology. Orthogonal inspection lines were drawn along the crack length, extending beyond the perceived crack tip. Relative displacements between the complex crack boundaries were calculated for each segment of the crack from the orthogonal lines. The differential displacements were used to determine convergence for each crack segment using equation 2.1.

3.2.2 DIC System Configuration and Specifications

To assist with data collection, a high contrast speckled surface pattern was applied to the specimen prior to collecting images. The web-gap region where cracking had developed was painted white, and a black marker was used to create a random, high contrast speckle pattern. Speckle diameters ranged from 1.5 to 2.0 mm (0.06 to 0.08 in.) and covered approximately 37% of the area of interest.

DIC data collection was conducted using two cameras spaced 214.3 mm (9.5 in.) apart with a 21.6° stereo angle. Before collecting DIC images, stereo calibration was performed for the two-camera setup. Calibration ensures the two cameras are in a known location relative to each other and the setup is capable of adequately analyzing out-of-plane displacements. Additionally, the calibration process helps to remove lens distortion and measurement bias, as well as defining a 3D coordinate system. The camera-to-specimen distance was approximately 508 mm (20.0 in.), similar to the setup shown in Figure 2.6(b). The cameras used for image collection were five-megapixel PGR Grasshopper3 cameras with a Sony IMX250 (CMOS) sensor and a frame rate of 75 frames per second. Schneider Xenoplan 1.4/17 mm Compact Series lenses were used with the cameras. External adjustable LED light panels were used to ensure the necessary contrast on the specimen surface and to prevent shadows.

To minimize noise and uncertainty in the DIC data, lighting, camera focus, and the speckle pattern were optimized. The cameras were focused to optimize the midrange focal length lenses, and lighting was determined to be 250 ± 35 lux. System accuracy was determined by computing confidence intervals to obtain Sigma-X, which represents one standard deviation of displacement uncertainty in the X-axis. Similar uncertainties can be found for the Y- and Z-axes, called Sigma-Y and Sigma-Z, respectively. It was found that idealized setup conditions resulted

in a Sigma-X that ranged from 0.0002 to 0.0022 mm (7.1e-6 to 8.5e-5 in.). Sigma-Y ranged from

0.0002 to 0.0031 mm (7.9e-6 to 1.2e-4 in.), and Sigma-Z ranged from 0.0004 to 0.0049 mm

(1.6e-5 to 1.9e-4 in.). The area where the cracks were located was in the lower bound of the

noise and uncertainty range, and these ranges were considered to be low within the context of the

crack lengths.

3.2.3 DIC Post-Processing

Two parameters used for DIC post-processing are the subset size and the step size. Subset

size is the width and height of the square of data being compared between the reference image

and deformed image. Step size is the distance between subset centers, which controls the spacing

of analysis. When analyzing the out-of-plane images, a subset size of 29 x 29 pixels was used,

and the step size was 7 pixels. These values for subset and step size resulted in low uncertainty

and a resolution level that was multiple orders of magnitude smaller than the crack sizes under

evaluation.

3.3 Complex Branched Distortion-Induced Fatigue Crack Results

3.3.1 Visualization of Results

Figure 3.4 shows the different strains obtained by the DIC software for the complex crack

pattern. The majority of the crack pattern is clearly visible in the strain images with the exception

of the last segment of the vertical crack, segment E-G, which was also difficult to visually detect.

While the von Mises strain (Figure 3.4f) showed the majority of the crack pattern, an important

note is that this computation does not convey differences between tensile and compression

regions of the crack. For example, the region surrounding the web-to-flange crack in Figure

3.4(f) is shown in red, but it is representative of compressive stresses, rather than tensile. A finite

element study found that the web-to-flange weld crack is under compression on the connection

plate side and under tension on the fascia side (Liu et al. 2015). Similarly, the maximum

principal strain is only capable of providing a clear picture of the entire crack pattern when

combined with the minimum principal strain.
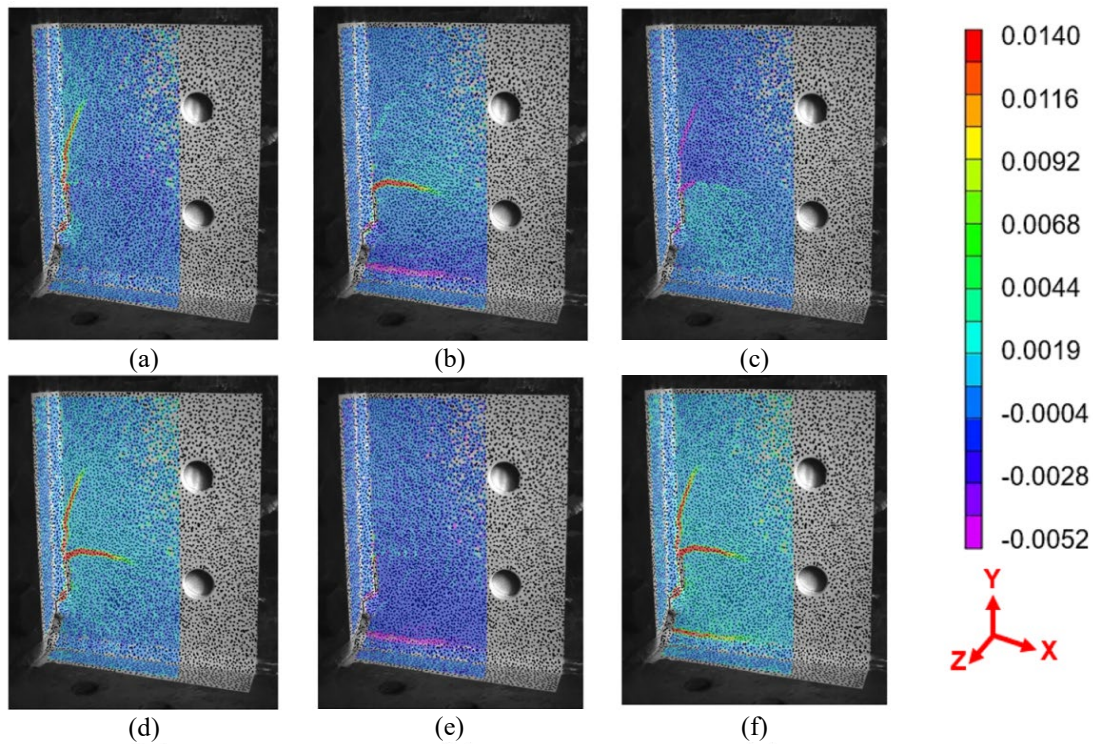
Figure 3.4 Typical visualized DIC strains: (a) strain in *x*-axis; (b) strain in *y*-axis; (c) strain in *xy*-plane; (d) max principal strain; (e) min principal strain; (f) von Mises strain

3.3.2 Crack Characterization Results

As previously described, differential displacements were computed along data extraction

lines arranged orthogonal to the crack path, and convergence for those displacements values was

calculated along the length of the crack path. Due to the complex geometry of the crack and the

web-gap region, displacements in all three principal directions were examined using DIC.

Additionally, the resultant differential displacement was calculated and evaluated for the crack

characterization methodology. The resultant displacement produced very similar trends and

magnitudes to the W-displacement since the W-displacement magnitude was significantly higher than the U- and V-displacement. Therefore, results based on the resultant displacement are not discussed in this report. Additionally, as the primary displacements were in the *yz*-plane, the U-displacement was found to have a significantly smaller magnitude than V- and W-displacements, creating a highly variable convergence curve for most loading cases. Therefore, the U-displacement data was not considered to be a useful indicator of crack location for this crack pattern.

The approach applied here was found to perform well under a broad range of applied loads, but a threshold to its applicability was identified as occurring at the lowest magnitude load case studied (LC1). Relative displacements in all three directions measured under LC1 were extremely small, resulting in highly variable convergence values and indicating the displacement-driven process was ineffective at this low load. Thus, this level of loading was identified as the threshold of applicability in the development of this approach. Data from LC1 is presented graphically in relative displacement and convergence plots, but is excluded from crack characterization methodologies. It should be noted that for most load cases, the relative displacements values in all the three directions approached zero well before the known crack tip location, resulting in an underprediction of crack length at 90% and 95% convergence values. For this reason, crack lengths at convergence values of 98% were also examined. Since both the 90% and 95% convergence data underpredicted crack length, the 90% convergence data was excluded from this report. The crack characterization results for each of the four crack segments are presented in the following sections.

3.3.3 Vertical Crack Characterization Results

The relative W- and V-displacements corresponding to the z- and y-directions for the vertical crack are presented visually in Figure 3.5 (a) and (c), respectively, with convergence curves for the same directions shown in Figure 3.5 (b) and (d). The length of the crack at segments B, C, D, E, and G, as determined through traditional visual inspection, are represented by the vertical dotted lines in the figures. In the y-direction, both relative displacement and convergence display a step-like trend for the diagonal second crack segment, B-C. This is caused by the low amount of vertical relative displacement occurring in the vertical segments on either side of B-C, compared with the much larger amount of vertical displacement within this segment.
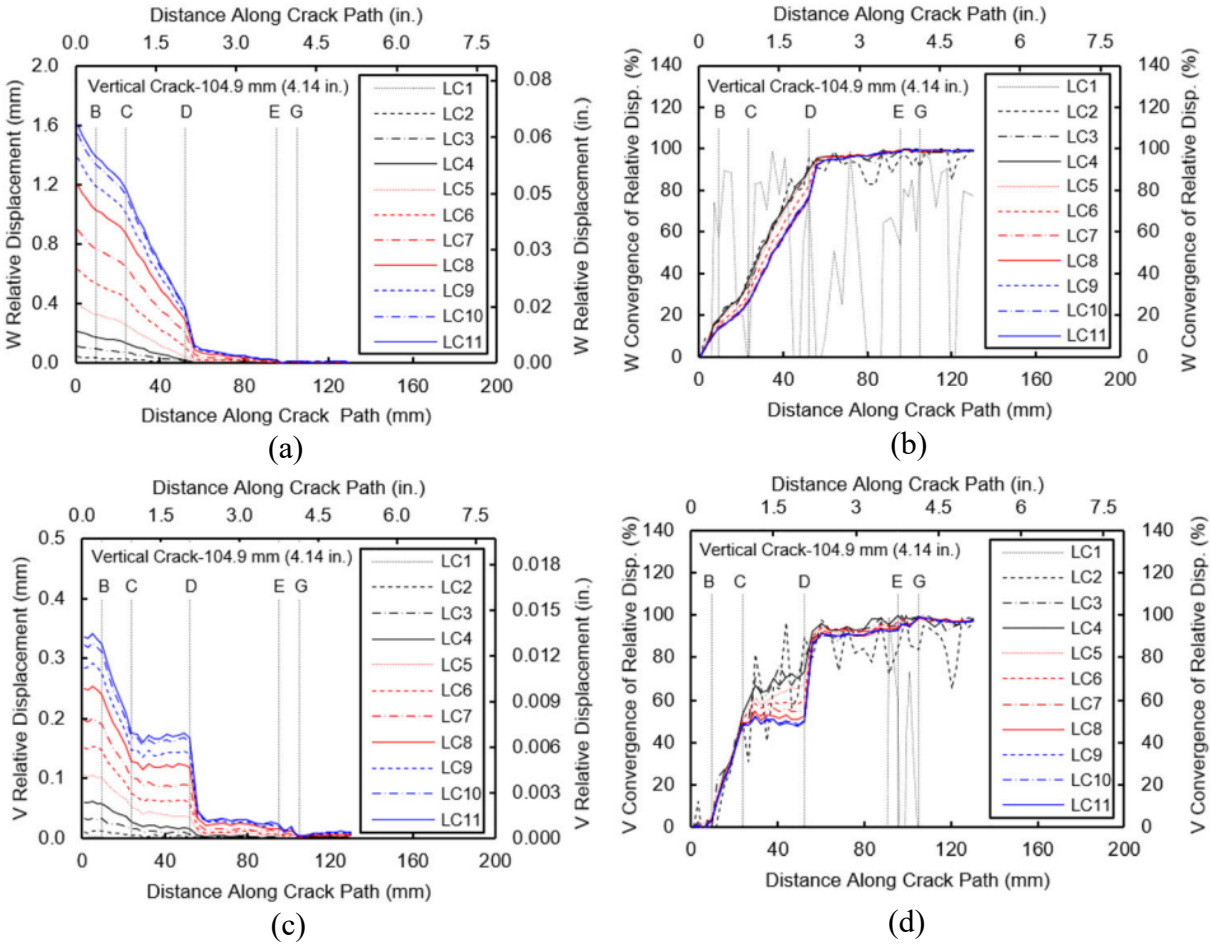
Figure 3.5 Vertical Crack: (a) relative W-displacement; (b) convergence of relative W-displacement; (c) relative V-displacement; (d) convergence of relative V-displacement

Tables 3.3 and 3.4 present the predicted crack lengths and the percent errors for the 95% and 98% convergence results compared with the visually measured crack length of 105 mm (4.14 in.). It can be seen that the 95% convergence values underpredicted the vertical crack lengths by an average of 42% based on the W-displacement and 17% based on the V-displacement. The 98% convergence resulted in a better prediction of the Vertical Crack length, with an average underprediction of 17% based on the W-displacement and 5% based on the V-

displacement. For load cases 6 through 11, with maximum forces between 13.3 to 24.5 kN (3.0 to 5.5 kip), the 98% convergence crack length was accurate to within 1%.

Table 3.3 Vertical Crack characterization for 95% convergence

Load Case	W-Displacement		V-Displacement	
	Length mm (in.)	Error	Length mm (in.)	Error
LC2	52.1 (2.05)	-50%	59.5 (2.34)	-43%
LC3	61.3 (2.41)	-42%	71.8 (2.83)	-32%
LC4	55.6 (2.19)	-47%	81.0 (3.19)	-23%
LC5	55.8 (2.20)	-47%	86.2 (3.39)	-18%
LC6	56.1 (2.21)	-47%	87.0 (3.43)	-17%
LC7	58.3 (2.30)	-44%	95.7 (3.77)	-9%
LC8	65.2 (2.57)	-38%	96.7 (3.81)	-8%
LC9	67.5 (2.66)	-36%	96.4 (3.80)	-8%
LC10	66.0 (2.60)	-37%	96.7 (3.81)	-8%
LC11	65.4 (2.57)	-38%	96.8 (3.81)	-8%
Avg.	**60.3 (2.37)**	**-42%**	**86.8 (3.42)**	**-17%**

Table 3.4 Vertical Crack characterization for 98% convergence

Load Case	W-Displacement		V-Displacement	
	Length mm (in.)	Error	Length mm (in.)	Error
LC2	87.3 (3.44)	-17%	98.8 (3.89)	-6%
LC3	87.2 (3.43)	-17%	86.9 (3.42)	-17%
LC4	85.3 (3.36)	-19%	83.6 (3.29)	-20%
LC5	86.1 (3.39)	-18%	98.2 (3.87)	-6%
LC6	86.2 (3.39)	-18%	104.9 (4.13)	0%
LC7	86.9 (3.42)	-17%	104.0 (4.09)	-1%
LC8	87.2 (3.43)	-17%	104.1 (4.10)	-1%
LC9	86.4 (3.40)	-18%	103.7 (4.08)	-1%
LC10	87.7 (3.45)	-16%	103.8 (4.09)	-1%
LC11	87.0 (3.43)	-17%	103.8 (4.09)	-1%
Avg.	**86.7 (3.41)**	**-17%**	**99.2 (3.91)**	**-5%**

3.3.4 Branched Crack I Characterization Results

The relative displacement and convergence values based on W- and V-displacements for Branched Crack I are shown in Figure 3.6. The length of the actual crack segments B, C, D, and F are represented by vertical dotted lines in the figures. The results based on V-direction displacement produce a step in the relative displacement and convergence curves for segment B-C. This flat section is caused by the large vertical displacements in the diagonal segment relative to the two vertical crack segments surrounding it.
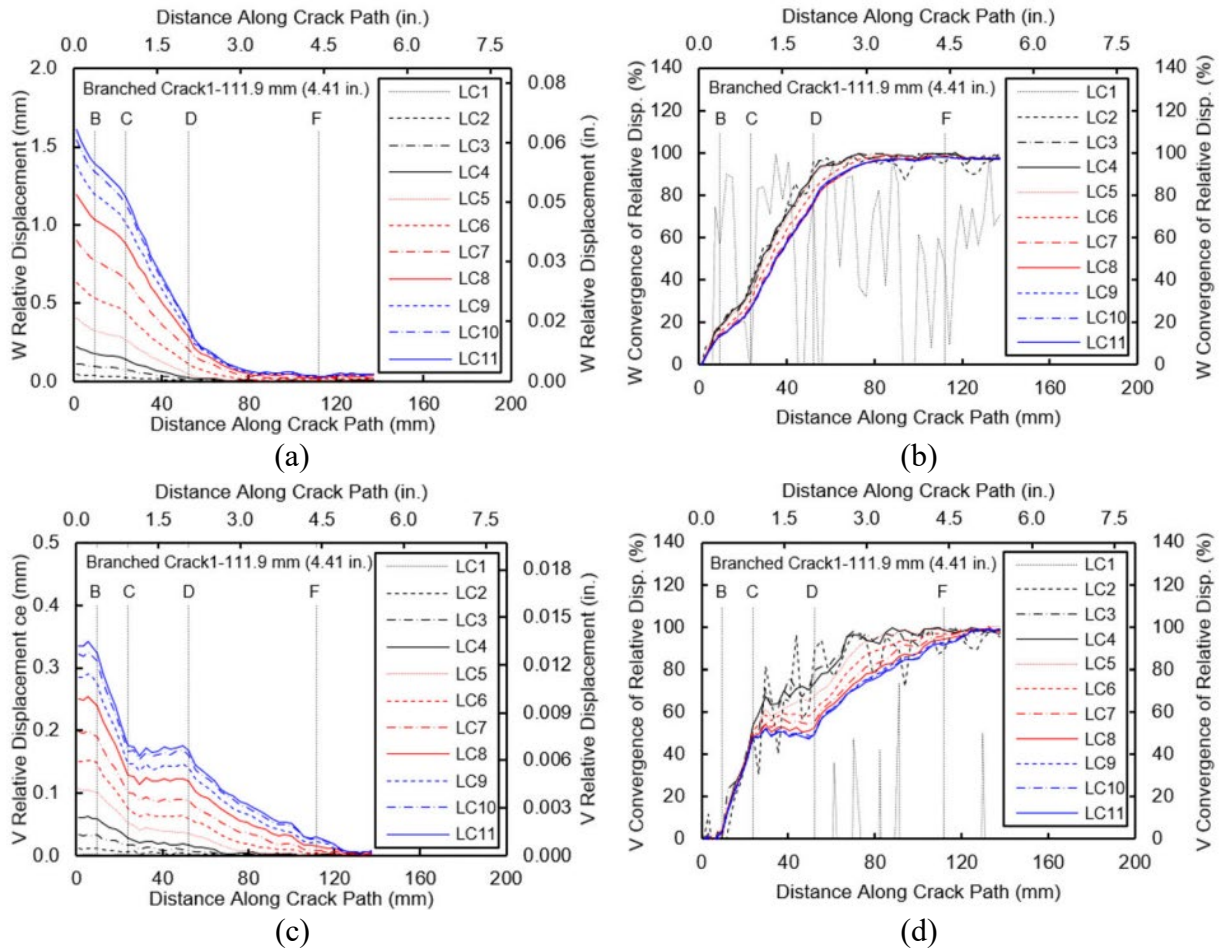

Figure 3.6 Branched Crack I: (a) relative W-displacement; (b) convergence of relative W-displacement; (c) relative V-displacement; (d) convergence of relative V-displacement

Tables 3.5 and 3.6 shows the predicted crack lengths and the percent error for 95% and 98% convergence compared with the visually measured Branched Crack I, which had a length of 112 mm (4.41 in.). Unlike the Vertical Crack, the length of Branched Crack I was under- and overestimated by the crack characterization methodology depending on the load case. The average error in predicted crack length was 39% based on W-displacement values and 14% based on V-displacement values for 95% convergence. The crack length estimates based on W-displacement were shorter than the measured crack length for all load cases, but the crack length based on the V-displacement slightly overestimated the crack length for load cases 8 through 11. By calculating the absolute value of the error for each load case, an average absolute error of 18% is obtained for the V-displacement estimates.

Evaluating crack lengths at 98% convergence resulted in significantly less errors based on W-displacement, with an average crack length across all eleven load cases of 111.4 mm (4.39 in.), an error of less than 1%. Individual load cases all have errors greater than 1% however, with an absolute average error of 13%. The 98% convergence results based on V-displacement are similar to the 95% convergence results, with load cases 2 through 6 underestimating crack length by 30% to 40% while crack length estimates from load cases 7 through 11 are accurate to within 6%. Due to the significant underestimation of the low load cases, the average error in the crack length estimate based on V-displacement is 19% for 98% convergence.

Table 3.5 Branched Crack I characterization for 95% convergence

Load Case	W-Displacement		V-Displacement	
	Length mm (in.)	Error	Length mm (in.)	Error
LC2	52.1 (2.05)	-53%	69.4 (2.73)	-38%
LC3	54.1 (2.13)	-52%	67.0 (2.64)	-40%
LC4	64.5 (2.54)	-42%	67.1 (2.64)	-40%
LC5	64.2 (2.53)	-43%	81.7 (3.22)	-27%
LC6	69.1 (2.72)	-38%	102.0 (4.02)	-9%
LC7	74.6 (2.94)	-33%	106.6 (4.20)	-5%
LC8	75.4 (2.97)	-33%	116.0 (4.57)	4%
LC9	75.6 (2.98)	-32%	118.4 (4.66)	6%
LC10	75.7 (2.98)	-32%	118.9 (4.68)	6%
LC11	75.9 (2.99)	-32%	120.1 (4.73)	7%
Avg.	**68.1 (2.68)**	**-39%**	**96.7 (3.81)**	**-14%**

Table 3.6 Branched Crack I characterization for 98% convergence

Load Case	W-Displacement		V-Displacement	
	Length mm (in.)	Error	Length mm (in.)	Error
LC2	105.2 (4.14)	-6%	69.5 (2.74)	-38%
LC3	90.8 (3.57)	-19%	68.5 (2.70)	-39%
LC4	86.1 (3.39)	-23%	68.5 (2.70)	-39%
LC5	90.3 (3.56)	-19%	71.5 (2.81)	-36%
LC6	119.1 (4.69)	6%	79.7 (3.14)	-29%
LC7	123.5 (4.86)	10%	105.0 (4.13)	-6%
LC8	124.4 (4.90)	11%	109.9 (4.33)	-2%
LC9	124.0 (4.88)	11%	110.2 (4.34)	-1%
LC10	124.8 (4.91)	11%	111.1 (4.37)	-1%
LC11	125.4 (4.94)	12%	111.0 (4.37)	-1%
Avg.	**111.4 (4.39)**	**-1%**	**90.5 (3.56)**	**-19%**

3.3.5 Branched Crack II Characterization Results

The relative displacements and convergence values for Branched Crack II are shown in

Figure 3.7. The vertical dotted lines in the figures represent the lengths of the actual crack

segments B, C, D, E, and H. There is a step-like trend for the vertical segment B-C for the
relative V-displacement and convergence due to the low relative vertical displacements for this
segment. Although segment E-H is not perfectly vertical, the step-like trend is also seen for this
segment for the same reason. This was confirmed by experimental observations, which indicated
the crack opening in segment E-H was very small and difficult to measure with dye penetrant.
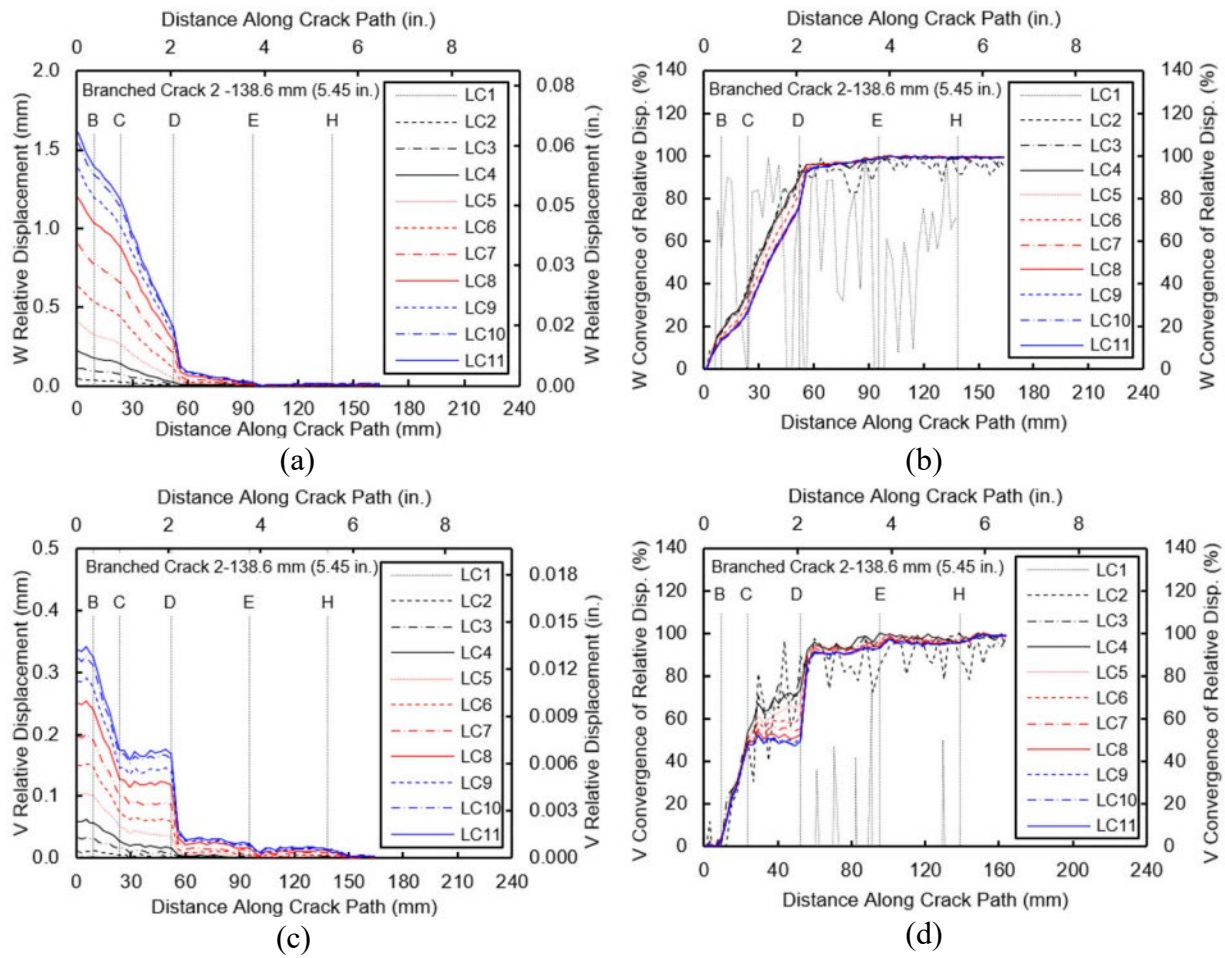

Figure 3.7 Branched Crack II: (a) relative W-displacement; (b) convergence of relative W-displacement; (c) relative V-displacement; (d) convergence of relative V-displacement

The predicted crack lengths and the percentage of error compared to the measured Branched Crack II length of 139 mm (5.45 in.) are shown in Tables 3.7 and 3.8 for 95% and 98% convergence, respectively. Based on W-displacement, both the 95% and 98% convergence results significantly underpredicted the crack length regardless of load case. The average error was 56% and 39% for the 95% and 98% convergence, respectively.

Similarly, the crack length was underestimated based on V-displacement for 95% convergence by an average of 37%. For the 98% convergence, the average crack length estimate is 123.2 mm (4.85 in.), an underestimation of 11%. The crack estimates for load cases 7 through 11 are slightly overestimated by approximately 5%, leading to an average absolute error of 17%.

Table 3.7 Branched Crack II characterization for 95% convergence

Load Case	W-Displacement		V-Displacement	
	Length mm (in.)	Error	Length mm (in.)	Error
LC2	52.1 (2.05)	-62%	59.5 (2.34)	-57%
LC3	61.3 (2.41)	-56%	71.8 (2.83)	-48%
LC4	55.6 (2.19)	-60%	81.0 (3.19)	-42%
LC5	55.8 (2.20)	-60%	86.2 (3.39)	-38%
LC6	56.1 (2.21)	-60%	87.0 (3.42)	-37%
LC7	58.3 (2.30)	-58%	95.7 (3.77)	-31%
LC8	65.2 (2.57)	-53%	96.9 (3.81)	-30%
LC9	67.5 (2.66)	-51%	97.9 (3.85)	-29%
LC10	66.0 (2.60)	-52%	97.3 (3.83)	-30%
LC11	65.4 (2.57)	-53%	97.4 (3.84)	-30%
Avg.	**60.3 (2.37)**	**-56%**	**87.1 (3.43)**	**-37%**

Table 3.8 Branched Crack II characterization for 98% convergence

Load Case	W-Displacement		V-Displacement	
	Length mm (in.)	Error	Length mm (in.)	Error
LC2	63.6 (2.50)	-54%	132.8 (5.23)	-4%
LC3	87.2 (3.43)	-37%	86.9 (3.42)	-37%
LC4	85.3 (3.36)	-38%	83.6 (3.29)	-40%
LC5	86.1 (3.39)	-38%	99.7 (3.93)	-28%
LC6	86.2 (3.39)	-38%	97.7 (3.85)	-30%
LC7	86.9 (3.42)	-37%	145.3 (5.72)	5%
LC8	87.2 (3.43)	-37%	147.1 (5.79)	6%
LC9	86.4 (3.40)	-38%	146.0 (5.75)	5%
LC10	87.7 (3.45)	-37%	147.4 (5.80)	6%
LC11	87.0 (3.43)	-37%	146.0 (5.75)	5%
Avg.	**84.4 (3.32)**	**-39%**	**123.2 (4.85)**	**-11%**

3.3.6 Horizontal Web-to-Flange Crack Characterization Results

The relative displacement and convergence values based on the V-direction for the horizontal web-to-flange crack are shown in Figure 3.8. The vertical dotted line in the figures represents the length of the actual web-to-flange crack of 51 mm (2.0 in.), based on visual inspection. The horizontal web-to-flange crack exhibited a high level of noise and did not converge well compared to the other cracks on the girder. U-, W-, and R- displacements were all found to be very noisy and did not approach the 95% convergence values expected. For the V-direction, over half of the displacement data sets did not approach 95% convergence.
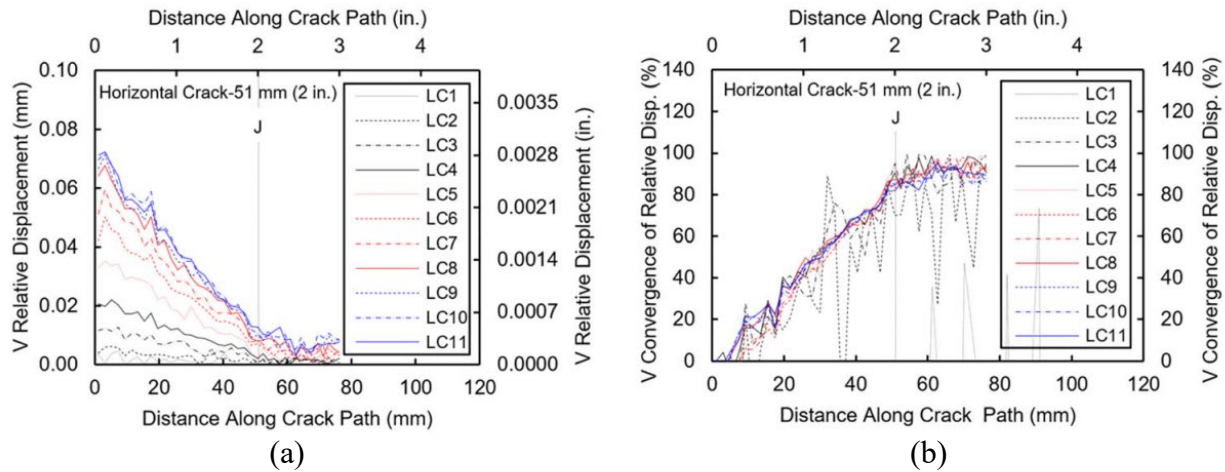
Figure 3.8 Horizontal web-to-flange crack: (a) relative V-displacement; (b) convergence of relative V-displacement

There are multiple explanations for the difficulty in characterizing the horizontal crack. First, relative displacements between the crack boundaries were very small. For example, the maximum relative W-displacements for the horizontal crack were found to be 0.08 mm (0.003 in.), compared to 1.6 mm (0.06 in.) for vertical and branched cracks. This corresponds with experimental observation, where the opening of the horizontal web-to-flange crack was extremely small and nearly invisible, making it very difficult to detect during visual inspection. Second, as discussed previously with regard to the strain visualization results, the horizontal crack is under compression on the interior side of the girder, producing crack closure under loading rather than opening. This behavior was confirmed with finite element analyses that showed the horizontal crack is under compression on the interior side of the girder and under tension on the fascia side. For these reasons, the horizontal web-to-flange was not able to be well-characterized using this DIC-based methodology, with convergence values never reaching 95% or 98%. Table 3.9 presents the calculated convergence percentage for each load case

associated with the actual crack length of 51.0 mm (2.0 in.). The average convergence at the

crack tip was 70% based on W-displacement and 86% based on V-displacement.

Table 3.9 Horizontal Crack characterization

Load Case	Convergence Percentage Associated with Actual Crack Length	
	W-Displacement	V-Displacement
LC2	47.4%	69.8%
LC3	63.0%	94.9%
LC4	86.9%	90.6%
LC5	74.6%	94.2%
LC6	81.7%	83.2%
LC7	75.8%	84.2%
LC8	66.3%	87.4%
LC9	69.1%	85.0%
LC10	66.4%	84.7%
LC11	67.3%	81.9%
Avg.	**69.9%**	**85.6%**

3.3.7 Complex Branched Distortion-Induced Fatigue Crack Summary

Figure 3.9 shows a visual summary for the predicted crack lengths and the corresponding

percent error for the Vertical Crack, Branched Crack I, and Branched Crack II. Figure 3.9(a)

shows the absolute average percent errors between the predicted and actual crack lengths for

95% and 98% convergence, while Figure 3.9(b) shows the predicted crack lengths based on the

95% and 98% convergence for relative V- and W-displacements. The dotted lines represent the

actual crack lengths.
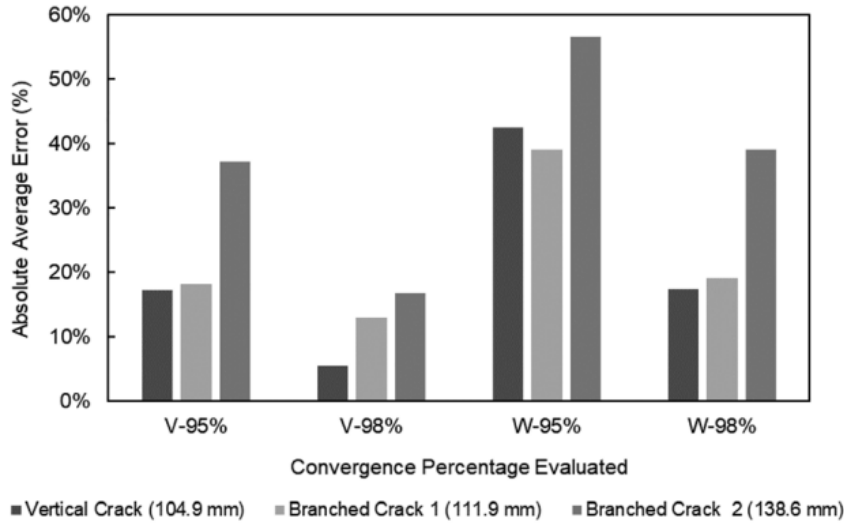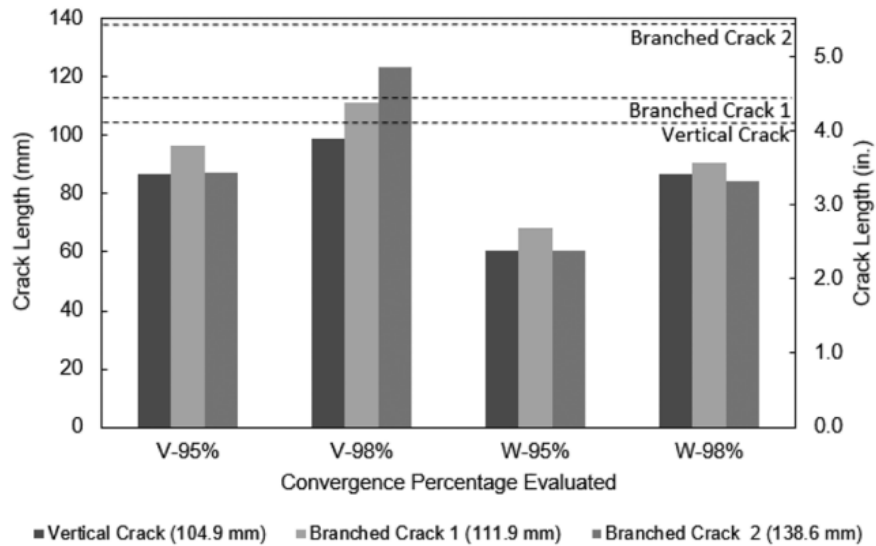
Figure 3.9 (a) Absolute average percent error between predicted and actual crack lengths for 95% and 98% convergence for relative V- and W-displacement; (b) predicted crack lengths based on 95% and 98% convergence for relative V- and W-displacement

For the Vertical and Branched cracks, the crack length estimates from 98% convergence exhibited reduced error compared to 95% convergence. It can also be seen that the crack length estimates based on V-displacement are more accurate than those based on W-displacement. For each crack, LC1, 2, and 3 produced very little crack opening, resulting in higher levels of error

when calculating convergence. The loading threshold where crack length prediction error

approaches 10% appears to be between LC4 and LC5 for the Vertical Crack, LC5 and LC6 for

Branched Crack I, and LC6 and LC7 for Branched Crack II. Lower load ranges did not produce

crack opening along the full crack length, making it difficult to detect the displacement

difference occurring at the crack tip, which resulted in crack length underestimation.

Chapter 4 Advancements Towards Automation

4.1 Distortion-Induced Fatigue Crack Single Camera Testing

4.1.1 Single Camera Testing Background

One of the constraints for applying the developed DIC testing methodology on in-service highway bridges is the limitations of an Unmanned Aerial Vehicle (UAV). The test setup for the developed methodology required two cameras, additional lighting panels, and highly idealized testing conditions. Reducing the number of cameras needed for one would result in a simplified testing setup as well as less weight acting on the UAV. The objective of this research was to evaluate the ability of a single camera to detect complex, distortion-induced cracking.

4.1.2 Single Camera Test Setup and Loading

DIC post-processing was performed using the original images collected during the initial out-of-plane distortion-induced fatigue testing. Images were obtained with a stereo camera setup, but were processed individually to provide two single-camera data sets with different angles. The crack pattern was made up of three linear segments, shown in Figure 4.1. The loading cases used were the same seven used for initial testing, with maximum forces ranging from 2.2 to 15.6 kN (0.5 to 3.5 kip), shown in Table 4.1. All loading cases had a minimum applied load of 0.9 kN (0.2 kip) to simulate the dead load of the bridge.
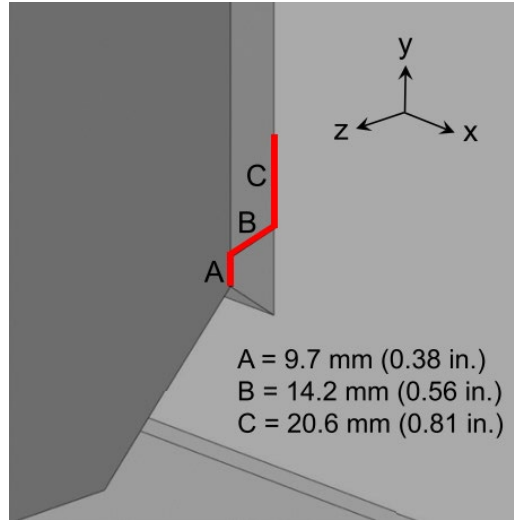
Figure 4.1 Crack location and geometry

Table 4.1 Single camera out-of-plane loading cases

Load Case	Load Range, kN (kip)	Displacement Range, mm (in.)
LC1	0.9 – 2.2 (0.2 – 0.5)	0.025 – 0.046 (0.001 – 0.002)
LC2	0.9 – 4.4 (0.2 – 1.0)	0.025 – 0.074 (0.001 – 0.003)
LC3	0.9 – 6.7 (0.2 – 1.5)	0.025 – 0.965 (0.001 – 0.038)
LC4	0.9 – 8.9 (0.2 – 2.0)	0.025 – 1.651 (0.001 – 0.065)
LC5	0.9 – 11.1 (0.2 – 2.5)	0.025 – 2.464 (0.001 – 0.097)
LC6	0.9 – 13.3 (0.2 – 3.0)	0.025 – 3.302 (0.001 – 0.130)
LC7	0.9 – 15.6 (0.2 – 3.5)	0.025 – 4.141 (0.001 – 0.163)

Post-processing of the images was performed in the VIC-2D software. While the original post-processing compared both images to determine an x-, y-, and z-axis relative displacement, the single camera testing found x- and y-axis relative displacement, U and V, respectively, for each camera angle, shown in Figure 4.2. The data from a single camera was then used to find convergence of relative displacement along the crack length. This was compared to the original convergence values to determine if a single camera can capture the complex crack location.
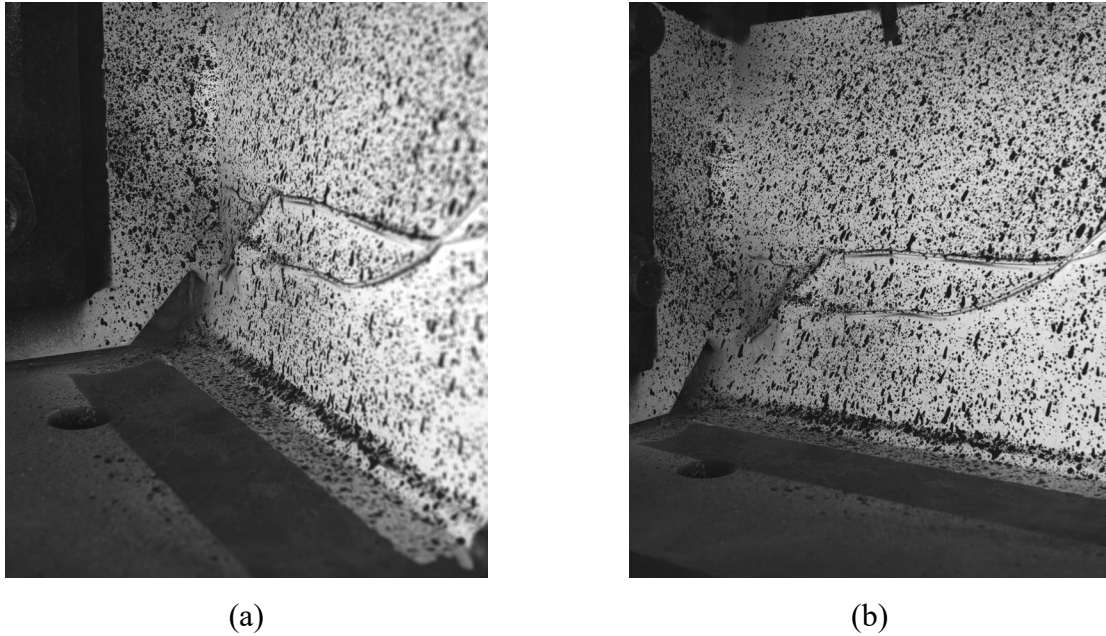
<center>(a)   (b)</center>

Figure 4.2 Cracked web gap region as seen from (a) camera 1 and (b) camera 2

4.1.3 Single Camera Results

The ability of a single camera DIC setup to capture the behavior of a complex, out-of-plane crack is highly dependent on the load case and which axis displacement is being evaluated on. Load cases 1 and 2 resulted in high amounts of noise in both the 2D and 3D setup, which made characterizing the crack challenging. Additionally, the results from the relative displacement in the V-direction was highly variable, with convergence frequently jumping and falling along the length of the crack. This can be seen visually for LC7 in Figure 4.3. Plots for load cases 1 through 6 are shown in Appendix B. The blue vertical lines represent the transition between different segments of the 44.5 mm (1.75 in.) crack and the crack tip. The red line shows the original data when processed using VIC-3D software. Crack estimates from the U-displacement are accurate for segments B and C of the crack, but do not detect segment A.
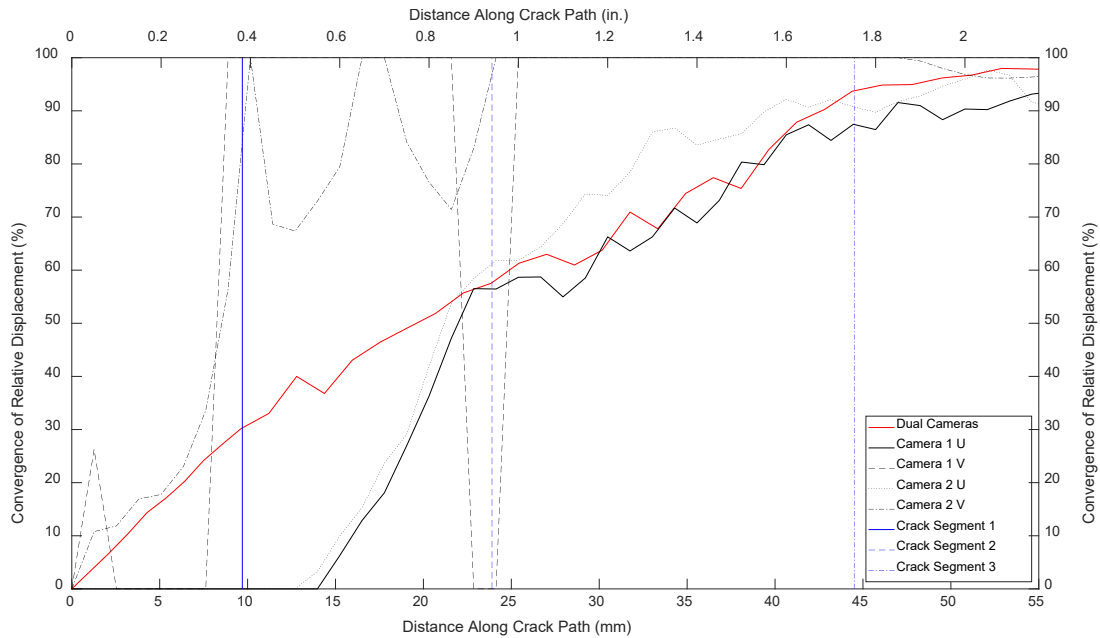
Figure 4.3 Convergence of relative displacement of a 44.5 mm (1.75 in.) complex crack under LC7

Another challenge with a single camera is that results are dependent on the camera angle. Table 4.2 shows the convergence at the crack tip based on relative U-displacement for both cameras and the change in convergence from the 3D analysis. For both 2D and 3D analysis, LC1 resulted in very noisy convergence plots that reached 100% convergence well before the crack tip, indicating a minimum threshold for applicability. As such, results for LC1 are not shown in Table 4.2. For load cases 2 through 7, the average convergence for camera 1 was 90.7%, while the average convergence for camera 2 was 90.9%. Compared to the average convergence from the 3D analysis of 94.1%, cameras 1 and 2 had an average error of 3.39% and 3.22%, respectively. These results indicate the 2D 95% convergence would overestimate the crack length.

Table 4.2 Convergence at 44.5 mm (1.75 in.) crack tip from U-displacement

Load Case	3D	Camera 1		Camera 2	
	Convergence	Convergence	Difference	Convergence	Difference
LC2	91.8%	93.9%	2.10%	91.8%	0.00%
LC3	97.4%	88.5%	-8.98%	92.3%	-5.13%
LC4	90.0%	90.4%	0.46%	97.4%	7.47%
LC5	95.6%	90.6%	-5.01%	90.5%	-5.12%
LC6	96.1%	90.2%	-5.87%	86.2%	-9.83%
LC7	93.9%	90.8%	-3.06%	87.2%	-6.68%
Avg.	**94.1%**	**90.7%**	**-3.39%**	**90.9%**	**-3.22%**

Average convergence for both cameras based on V-displacement was much higher than for U-displacement, but this was primarily due to the convergence jumping to 100% early along the crack path and remaining there, indicating that convergence in the V-direction was not an effective indicator of crack length regardless of the camera angle. Therefore, results for the V-direction are not shown in this report.

Initial results show that a single camera can detect the behavior of the crack path but is highly dependent upon the direction of the analysis, the camera angle, and the load that the crack is subjected to. Additional research will be needed to determine exactly how important camera angle is when utilizing a single camera, particularly since the angle was not measured during this testing. While the camera that captured the crack behavior was looking "directly" at the crack, it was not quantified and was highly subjective. Single-camera DIC results should be evaluated more thoroughly, particularly under varying light and focus conditions, and different UAV alternatives should be assessed to determine whether a UAV would be equipped to carry a stereo camera setup.

Chapter 5 Conclusions and Future Work

5.1 Conclusions

This report summarizes the ability of a previously developed DIC-based methodology for characterizing geometrically complex bifurcated DIF cracks in steel bridges. The methodology utilizes relative displacement between crack edges to determine the crack length. The methodology was successful at characterizing bifurcated cracks propagating in the girder web, but characterization of a horizontal crack at the web-to-flange connection was found to be a limitation of the technique. The following conclusions have been drawn from the study:

1. A convergence of 98% was found to provide a more accurate estimation of the crack length on a steel girder loaded out-of-plane with complex fatigue crack geometry compared with 95% convergence. Due to this increased accuracy, 98% convergence is recommended for crack length characterization when used with similar crack patterns and applications.

2. The methodology was found to result in more accurate results when V-direction displacements were used rather than U- and W-direction displacements, which can be attributed to the V-direction corresponding to the direction of loading.

3. On average, 98% convergence based on V-direction displacement data resulted in underprediction of crack lengths with 5%, 13%, and 17% error for the Vertical Crack, Branched Crack I, and Branched Crack II, respectively.

4. The crack characterization methodology was found to not converge well for the horizontal web-to-flange crack under this mode of loading. This was because the web-to-flange crack experienced crack closure on the interior face of the girder, and relative displacements were extremely small along the crack length.

5. Load cases with low load levels resulted in a greater error in terms of crack length determination. The threshold of adequate loading for use with this technique appears to be between LC4 and LC5 for the Vertical Crack, LC5 and LC6 for Branched Crack I, and LC6 and LC7 for Branched Crack II, as load levels below this did not produce a crack opening along the full length of the crack.

The same DIF test setup was also used to evaluate the ability of a single camera to accurately identify out-of-plane cracks. It was found that a single-camera DIC was capable of accurately estimating the crack length at approximately 90% convergence, but results are highly dependent on the analysis direction and the angle of the crack. Similar to the 3D analysis, LC1 with a maximum load of 2.2 kN (0.5 kip) provided an insufficient crack opening, indicating a minimum threshold of applicability.

5.2 Future Work

For the proposed methodology to be employed for in-service inspections of highway bridges, the associated hands-on work needs to be minimized. As the described work is still an early step towards using DIC in this application, it is recognized that additional work is needed to realize the potential of the system. Ongoing work is examining the necessity of the painted-on high contrast pattern, instead utilizing existing surface defects for DIC analysis. Additional ongoing work is examining the limitations of the methodology discussed in this paper, primarily regarding the idealized light and focus conditions necessary for detecting and characterizing fatigue cracks. Identifying and characterizing DIF cracks using an automated methodology that does not rely on hands-on human visual inspection would benefit bridge owners and stakeholders as it has the potential to decrease the time and cost of performing inspections, as well as reduce

the risk for inspectors and the traveling public. This methodology could potentially be used as a stand-alone tool, in conjunction with other inspection techniques, and/or as an early warning that will trigger more invasive manual inspections. Work described in this paper constitutes an important step to accomplishing this goal.

References

Abdel-Qader, I., Abudayyeh, O., & Kelly, M. E. (2003). Analysis of edge-detection techniques for crack identification in bridges. *J. Comp. Civil Eng.*, 17(4), 255-263.

Alipour, M., Washlesky, S. J., & Harris, D. K. (2019). Field Deployment and Laboratory Evaluation of 2D Digital Image Correlation for Deflection Sensing in Complex Environments. *J. Bridge Eng.*, 24(4), 04019010. doi: 10.1061/(ASCE)BE.1943-5592.0001363.

Al-Salih, H., Juno, M., Collins, W., Bennett, C., Li, J., & Sutley, E. (2019). Evaluation of a Digital Image Correlation Bridge Inspection Methodology on Complex Distortion-Induced Fatigue Cracking. *In Procedia Structural Integrity*, 17, 682-689.

Al-Salih, H., Juno, M., Collins, W., Bennett, C., & Li, J. (2021). Application of a digital image correlation bridge inspection methodology on geometrically complex bifurcated distortion-induced fatigue cracking. *Fatigue Fract. Eng. Mater. Struct.*, 1-16. doi: 10.1111/ffe.13453.

American Society of Civil Engineers (ASCE). (2021). 2021 Infrastructure Report Card – Bridges, https://www.infrastructurereportcard.org/wp-content/uploads/2020/12/Bridges-2021.pdf.

Blaber, J., Adair, B., and Antoniou, A. (2015). Ncorr: Open-Source 2D Digital Image Correlation Matlab Software. *Exp. Mech.*, 55, 1105-1122. doi: 10.1007/s11340-015-0009-1.

Campbell, L. E., Connor, R. J., Whitehead, J. M., & Washer, G. A. (2020). Benchmark for Evaluating Performance in Visual Inspection of Fatigue Cracking in Steel Bridges. *J. Bridge Eng.*, 25(1). doi: 10.1061/(ASCE)BE.1943-5592.0001507.

Carroll, J., Abuzaid, W., Lambros, J., & Sehitoglu, H. (2012). High resolution digital image correlation measurements of strain accumulation in fatigue crack growth. *Int. J. Fatigue*. doi: 10.1016/j.ijfatigue.2012.06.010.

Carroll, J., Efstathiou, C., Lambros, J., Sehitoglu, H., Hauber, B., Spottswood, S. & Chona, R. (2009). Investigation of fatigue crack closure using multiscale image correlation experiments. *Eng. Fract. Mech.*, 76(15): 2384.

Cha, Y. J., Choi, W., & Büyüköztürk, O. (2017). Deep Learning-Based Crack Damage Detection Using Convolutional Neural Networks. *Comp.-Aided Civil Infrastruct. Eng.*, 32(5), 361-378.

Chen, F., Chen, X., Xie, X., Feng, X., & Yang, L. (2013). Full-field 3D measurement using multi-camera digital image correlation system. *Opt. Lasers Eng.*, 51(9), 1044-1052. doi: 10.1016/j.optlaseng.2013.03.001.

Cigada, A., Mazzoleni, P., & Zappa, E. (2014). Vibration monitoring of multiple bridge points by means of a unique vision-based measuring system. *Exp. Mech.*, 54(2), 255-271.

Connor, R. J., & Fisher, J. W. (2006). Identifying effective and ineffective retrofits for distortion fatigue cracking in steel bridges using field instrumentation. *J. Bridge Eng.*, 11(6), 745-752.

Dellenbaugh, L., Kong, X., Al-Salih, H., Collins, W., Bennett, C., Li, J., & Sutley, E. (2020). "Development of Distortion-Induced Fatigue Crack Characterization Methodology using Digital Image Correlation." *J. Bridge Eng.*, 25(9). doi: 10.1061(ASCE)BE.1943-5592.0001598.

Dhanasekar, M., Prasad, P., Dorji, J., & Zahra, T. (2018). Serviceability Assessment of Masonry Arch Bridges Using Digital Image Correlation. *J. Bridge Eng.*, 24(2), 04018120. doi: 10.1061/(ASCE)BE.1943-5592.0001341.

Federal Highway Administration (FHWA). (2004). *National bridge inspection standards*, Federal Register, 69 (239).

Fisher, J. W. (1984). *Fatigue and fracture in steel bridges. Case studies*. J. Wiley and Sons, Limited; Sussex, England.

Hamam, R., Hild, F., & Roux, S. (2007). Stress Intensity Factor Gauging by Digital Image Correlation: Application in Cyclic Fatigue. *Strain*, 43(3), 181-192. doi: 10.1111/j.1475-1305.2007.00345.x.

Helfrick, M. N., Niezrecki, C., Avitabile, P., & Schmidt, T. (2011). 3D digital image correlation methods for full-field vibration measurement. *Mech. Systems and Signal Processing*, 25(3), 917-927. doi: 10.1016/j.ymssp.2010.08.013.

Helm, J. D. (1996). Improved three-dimensional image correlation for surface displacement measurement. *Opt. Eng.*, 35(7), 1911. doi: 10.1117/1.600624.

Hutt, T., & Cawley, P. (2009). Feasibility of digital image correlation for detection of cracks at fastener holes. *NDT & E International*. 42, 141-149. doi: 10.1016/j.ndteint.2008.10.008.

International Digital Image Correlation Society, Jones, E. M. C., & Iadicola, M. A. (Eds.). (2018). A Good Practice Guide for Digital Image Correlation. doi: 10.32720/idics/gpg.ed1.

Juno, M., Al-Salih, H., Collins, W., Bennett, C., Li, J., & Sutley, E. (2020). Investigating lighting and focus limitations of digital image correlation as a bridge inspection tool. *Structures Congress 2020*, 341-348. doi: 10.1061/9780784482896.032.

Kong, X., & Li, J. (2018). Vision-based Fatigue Crack Detection of Steel Structures Using Video Feature Tracking. *Comp.-Aided Civil Infrastruct. Eng.*, 33(9), 783-799.

Küntz, M., Jolin, M., Bastien, J., Perez, F., & Hild, F. (2006). Digital image correlation analysis of crack behavior in a reinforced concrete beam during a load test. *Canadian J. Civil Eng.*, 33(11), 1418-1425. doi: 10.1139/l06-106.

Lee, J. J., & Shinozuka, M. (2006). A vision-based system for remote sensing of bridge displacement. *NDT & E International*, 39(5), 425-431. doi: 10.1016/j.ndteint.2005.12.003.

Liu, H. In: Bennett, C. R., Li, J., Matamoros, A., Rolfe, S., & Ward, D., (Eds). (2015). A Finite-Element-Based Approach to Modeling Cracking & Repairs for Distortion-Induced Fatigue in Steel Bridges. *ProQuest Dissertations Publishing.*

Lorenzino, P., Beretta, G., & Navarro, A. (2014). Application of Digital Image Correlation (DIC) in resonance machines for measuring fatigue crack growth. *Frattura ed Integrità Strutturale.* 30, 369-374. doi: 10.3221/IGF-ESIS.30.44.

Nowell, D., Paynter, R. J., & Matos, P. F. (2010). Optical methods for measurement of fatigue crack closure: Moiré interferometry and digital image correlation. *Fatigue & Fracture of Engineering Materials & Structures*, 33(12), 778-790. doi: 10.1111/j.1460-2695.2010.01447.x

Pan, B., Tian, L., & Song, X. (2016). Real-time, non-contact and targetless measurement of vertical deflection of bridges using off-axis digital image correlation. *NDT & E International*, 79, 73-80. doi: 10.1016/j.ndteint.2015.12.006

Reagan, D., Sabato, A., & Niezrecki, C. (2018). Feasibility of using digital image correlation for unmanned aerial vehicle structural health monitoring of bridges. *Structural Health Monitoring*, *17*(5), 1056–1072. doi: 10.1177/1475921717735326

Ribeiro, D., Calçada, R., Ferreira, J., & Martins, T. (2014). Non-contact measurement of the dynamic displacement of railway bridges using an advanced video-based system. *Engineering Structures*, 75, 164-180. doi: 10.1016/j.engstruct.2014.04.051

Rupil, J., Roux, S., Hild, F., & Vincent, L. (2011). Fatigue microcrack detection with digital image correlation. *The Journal of Strain Analysis for Engineering Design*. 46. 492-509. doi: 10.1177/0309324711402764.

Sutton, M. A., Yan, J. H., Deng, X., Cheng, C. S., & Zavattieri, P. (2007). Three-dimensional digital image correlation to quantify deformation and crack-opening displacement in ductile aluminum under mixed-mode I/III loading. *Optical Engineering*, 46(5), 051003. doi: 10.1117/1.2741279.

Turner, D. Z. (2015.) Digital Image Correlation Engine (DICe) Reference Manual. Sandia Nat. Lab.: Livermore, California, USA. http://dicengine.github.io/dice/.

Vanlanduit, S., Vanherzeele, R., Longo, R., & Guillaume, P. (2008). Investigation of fatigue cracks using digital image correlation. *Emerging Technologies in NDT*. 4, 53-58.

Vanlanduit, S., Vanherzeele, R., Longo, R., & Guillaume, P. (2009). A digital image correlation method for fatigue test experiments. *Optics and Lasers in Engineering*, 47(3-4), 371-378. doi: 10.1016/j.optlasend.2008.03.016.

Whitehead, J. (2015). "Probability of detection study for visual inspection of steel bridges." Master's Thesis, Purdue University, West Lafayette, IN.

Yamaguchi, T., & Hashimoto, S. (2010). Fast crack detection method for large-size concrete surface images using percolation-based image processing. *Machine Vision and Applications*, 21(5), 797-809.

Yang, J., & Bhattacharya, K. (2020). Augmented Lagrangian Digital Image Correlation (AL-DIC) Code Manual. CaltechDATA. doi: 10.22002/D1.1443.

Yeum, C. M., & Dyke, S. J. (2015). Vision-based automated crack detection for bridge inspection. *Comp.-Aided Civil Infrastruct. Eng.*, 30(10), 759-770.

Yu, S. N., Jang, J. H., & Han, C. S. (2007). Auto inspection system using a mobile robot for detecting concrete cracks in a tunnel. *Automation in Construction*, 16(3), 255-261.

Yuan, Y., Huang, J., Peng, X., Xiong, C., Fang, J., & Yuan, F. (2014). Accurate displacement measurement via a self-adaptive digital image correlation method based on a weighted ZNSSD criterion. *Opt. Lasers Eng.*, 52, 75-85. doi: 10.1016/j.optlaseng.2013.07.016.

Zhang, R., & He, L. (2012). Measurement of mixed-mode stress intensity factors using digital image correlation method. *Opt. Lasers Eng.*, 50(7), 1001-1007. doi: 10.1016/j.optlaseng.2012.01.009.

Zhao Z., & Haldar, A. (1996). Bridge fatigue damage evaluation and updating using non-destructive inspections. *Eng. Fracture Mech.*, 53(5), 775-88.

Zhao, Y., & Roddis, W. M. K. (2004). Fatigue Prone Steel Bridge Details: Investigation and Recommended Repairs, *K-TRAN: KU-99-2, Final Report.* Kansas Department of Transportation, Topeka, KS.

Zou, Q., Cao, Y., Li, Q., Mao, Q., & Wang, S. (2012). CrackTree: Automatic crack detection from pavement images. *Pattern Recognition Letters*, 33(3), 227-238.

Appendix A Previous Work

Tables A.1 through A.3 show the light and focus testing conditions for camera to specimen distances of 648, 432, and 216 mm (25.5, 17.0, and 8.5 in.), respectively.

Table A.1 Light and focus conditions for 648 mm (25.5 in.) distance

Condition	Focus	Focal Length, mm (in.)	Lighting	Light Range, lumens
1	Ideal	648 (25.5)	High	5850 – 6600
2	Ideal	648 (25.5)	Medium	4450 – 5000
3	Ideal	648 (25.5)	Low	2000 – 2350
4	Fair	615 (24.2)	High	5850 – 6600
5	Fair	615 (24.2)	Medium	4450 – 5000
6	Poor	583 (22.9)	High	5850 – 6600

Table A.2 Light and focus conditions for 432 mm (17.0 in.) distance

Condition	Focus	Focal Length, mm (in.)	Lighting	Light Range, lumens
1	Ideal	432 (17.0)	High	5850 – 6600
2	Ideal	432 (17.0)	Medium	4450 – 5000
3	Ideal	432 (17.0)	Low	2000 – 2350
4	Fair	410 (16.2)	High	5850 – 6600
5	Fair	410 (16.2)	Medium	4450 – 5000
6	Poor	389 (15.3)	High	5850 – 6600

Table A.3 Light and focus conditions for 216 mm (8.5 in.) distance

Condition	Focus	Focal Length, mm (in.)	Lighting	Light Range, lumens
1	Ideal	216 (8.5)	High	5850 – 6600
2	Ideal	216 (8.5)	Medium	4450 – 5000
3	Ideal	216 (8.5)	Low	2000 – 2350
4	Fair	205 (8.1)	High	5850 – 6600
5	Fair	205 (8.1)	Medium	4450 – 5000
6	Poor	195 (7.7)	High	5850 – 6600

Typical DIC results for each camera to specimen distances are shown in Figures A.1 through A.6. This shows the comparison between more and less ideal conditions.

(a)   (b)
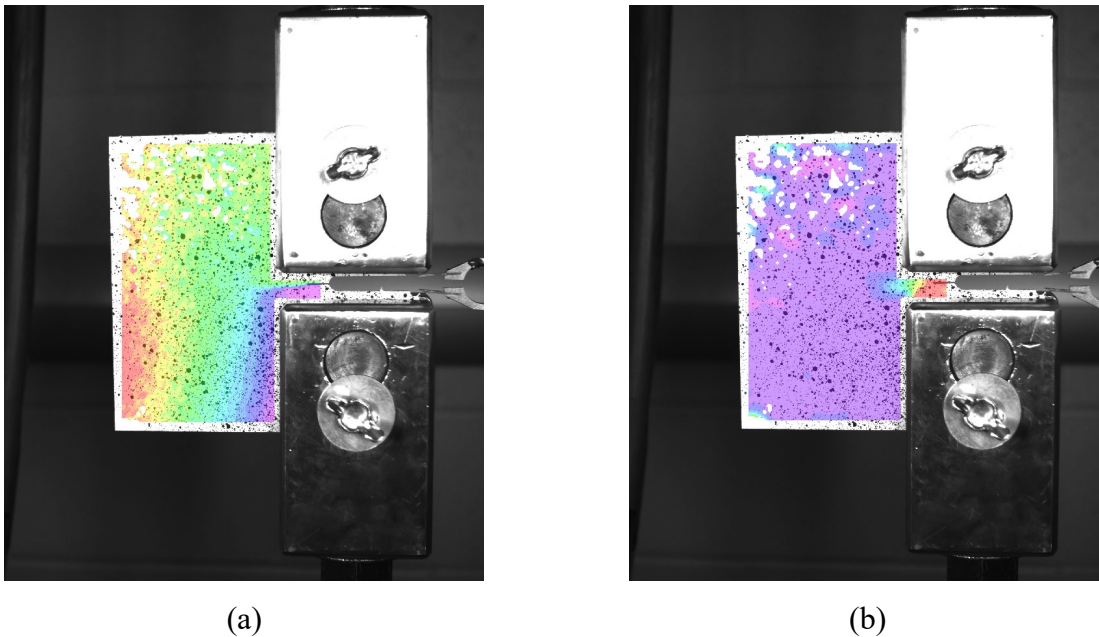
Figure A.1 DIC results for a 25.4 mm (1.0 in.) crack with 648 mm (25.5 in.) camera distance under LC5 and Condition 1 in terms of (a) displacement and (b) strain
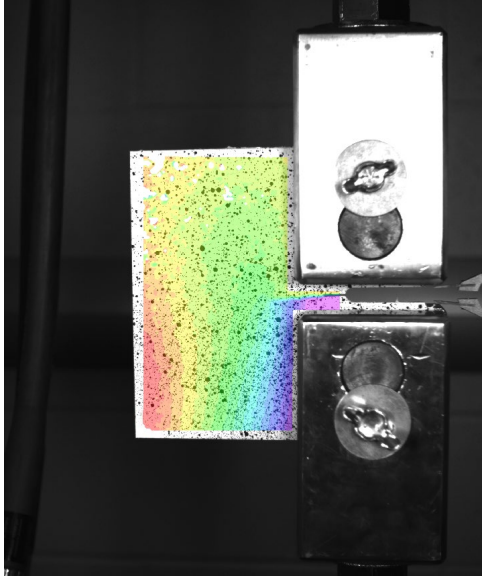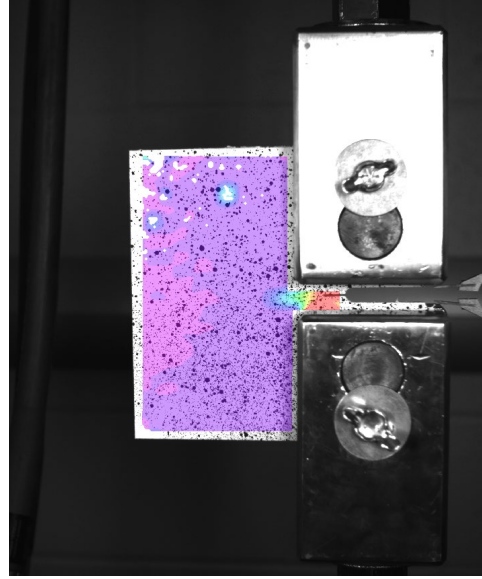
(a)   (b)

Figure A.2 DIC results for a 25.4 mm (1.0 in.) crack with 648 mm (25.5 in.) camera distance under LC5 and Condition 5 in terms of (a) displacement and (b) strain
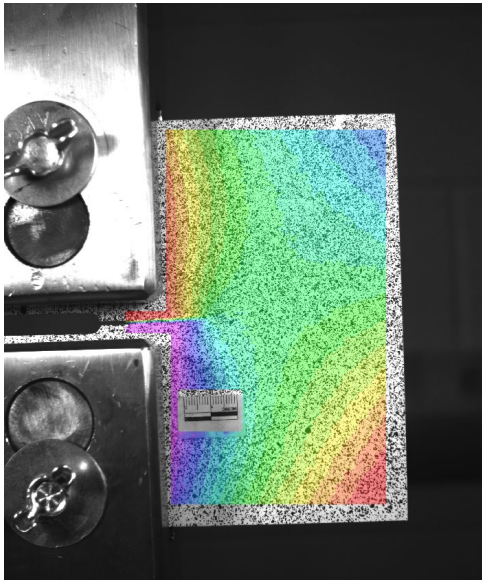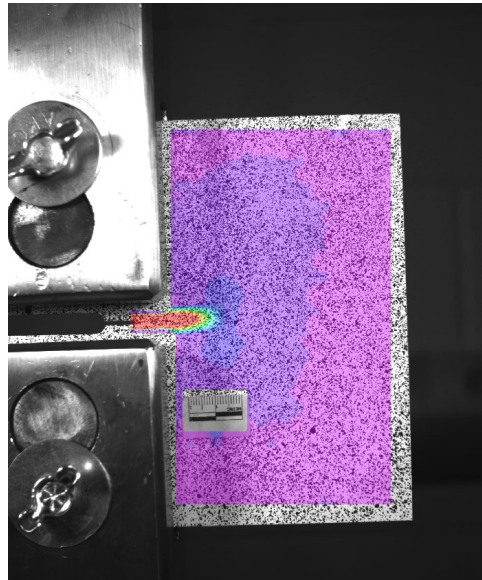
(a)   (b)

Figure A.3 DIC results for a 25.4 mm (1.0 in.) crack with 432 mm (17.0 in.) camera distance under LC5 and Condition 1 in terms of (a) displacement and (b) strain
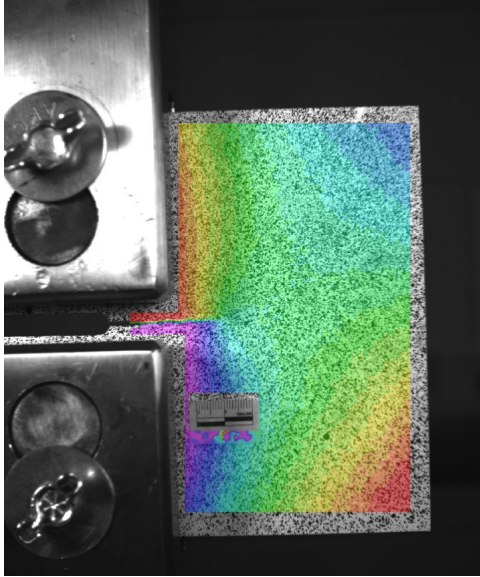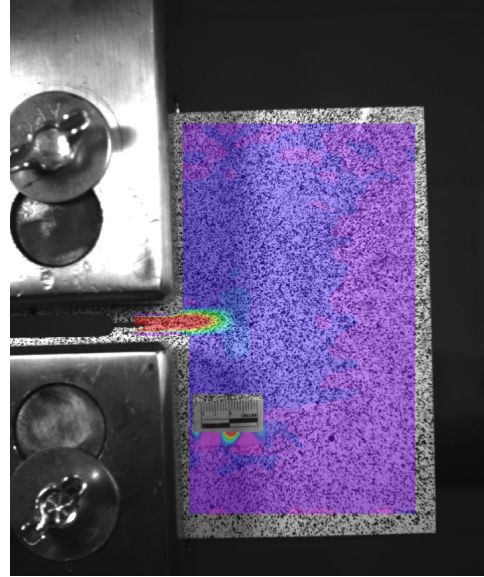
(a)   (b)

Figure A.4 DIC results for a 25.4 mm (1.0 in.) crack with 432 mm (17.0 in.) camera distance under LC5 and Condition 5 in terms of (a) displacement and (b) strain
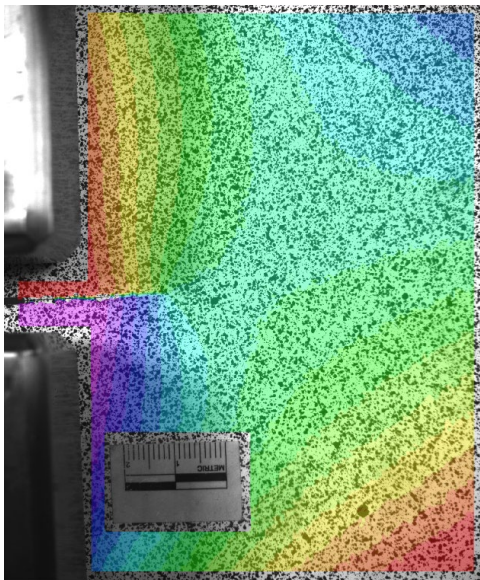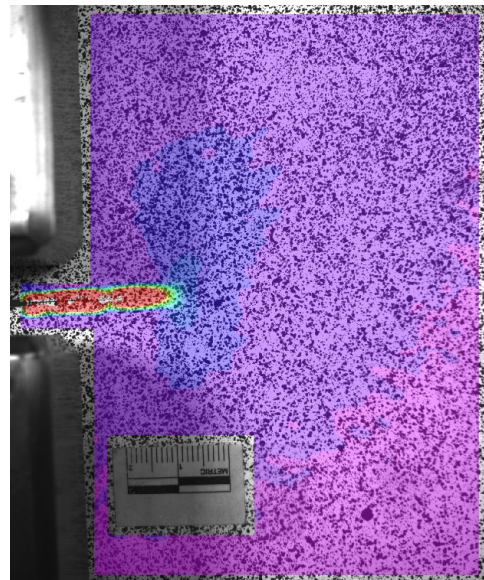
(a)   (b)

Figure A.5 DIC results for a 25.4 mm (1.0 in.) crack with 216 mm (8.5 in.) camera distance under LC5 and Condition 1 in terms of (a) displacement and (b) strain

<center>(a)   (b)</center>
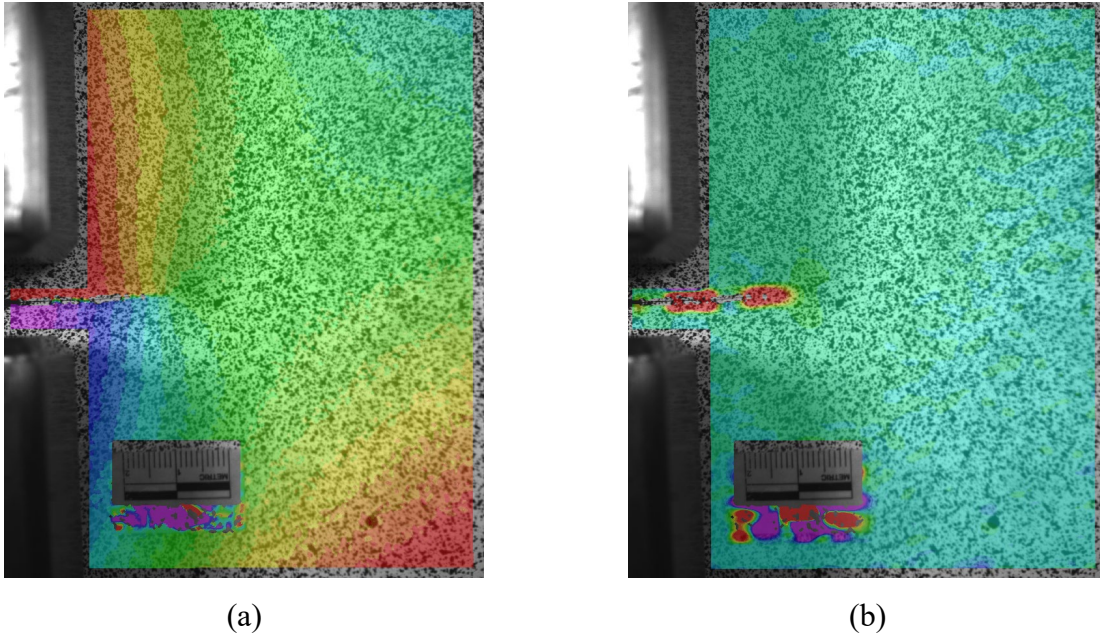
Figure A.6 DIC results for a 25.4 mm (1.0 in.) crack with 216 mm (8.5 in.) camera distance under LC5 and Condition 5 in terms of (a) displacement and (b) strain

The relative displacement and convergence for each camera to specimen distance is shown in figures A.7 through A.12. These are representative of each load case evaluated.
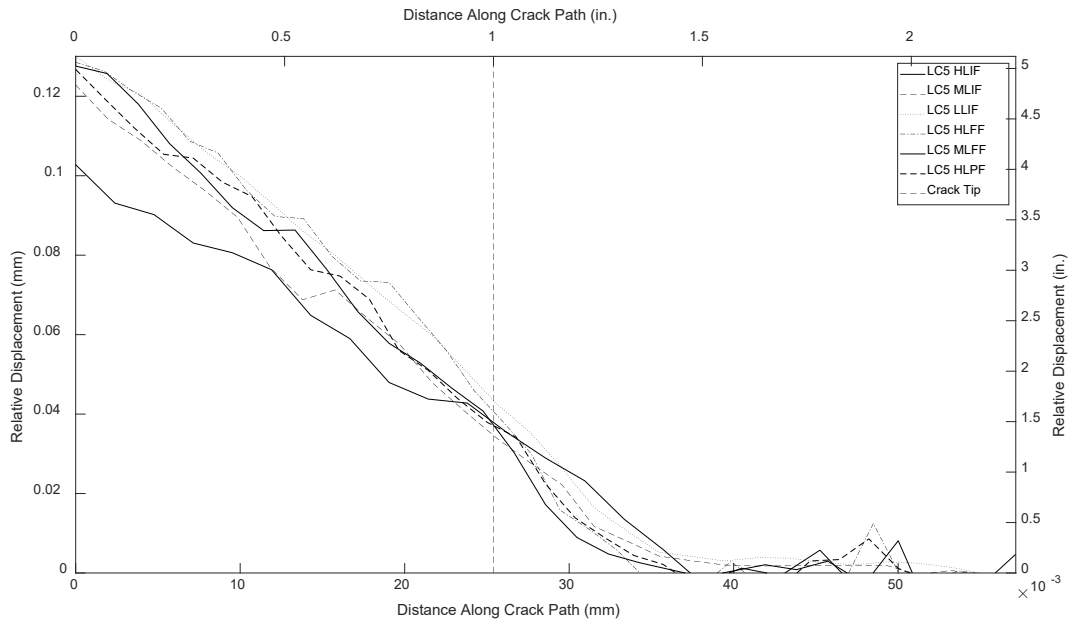
Figure A.7 Relative displacement of a 25.4 mm (1.0 in.) crack with a camera distance of 648 mm (25.5 in.) under LC5
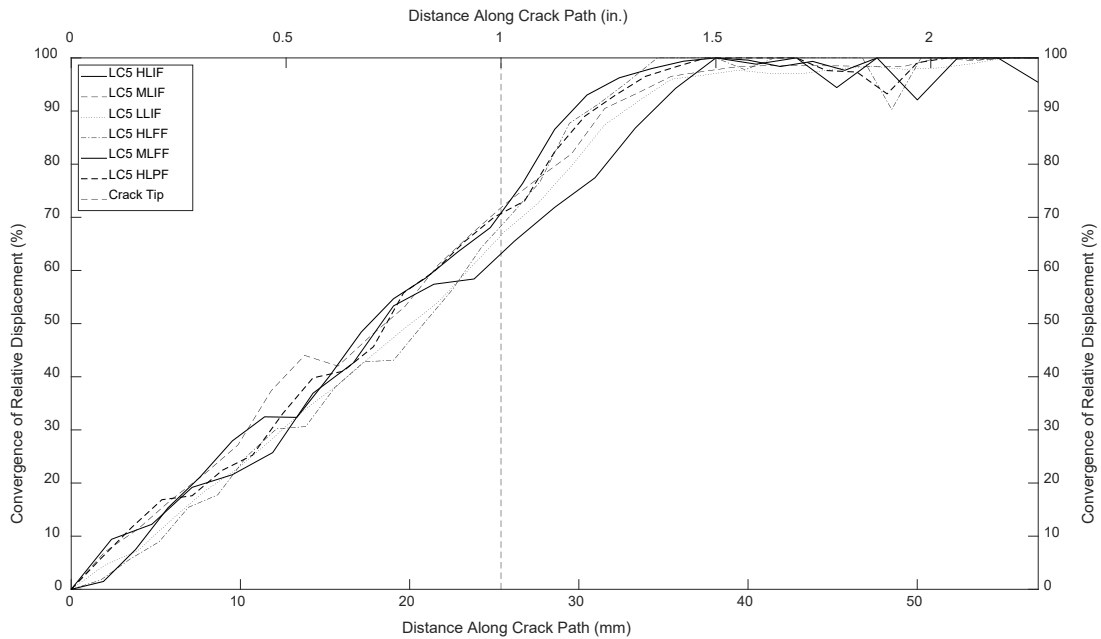
Figure A.8 Convergence of relative displacement of a 25.4 mm (1.0 in.) crack with a camera distance of 648 mm (25.5 in.) under LC5
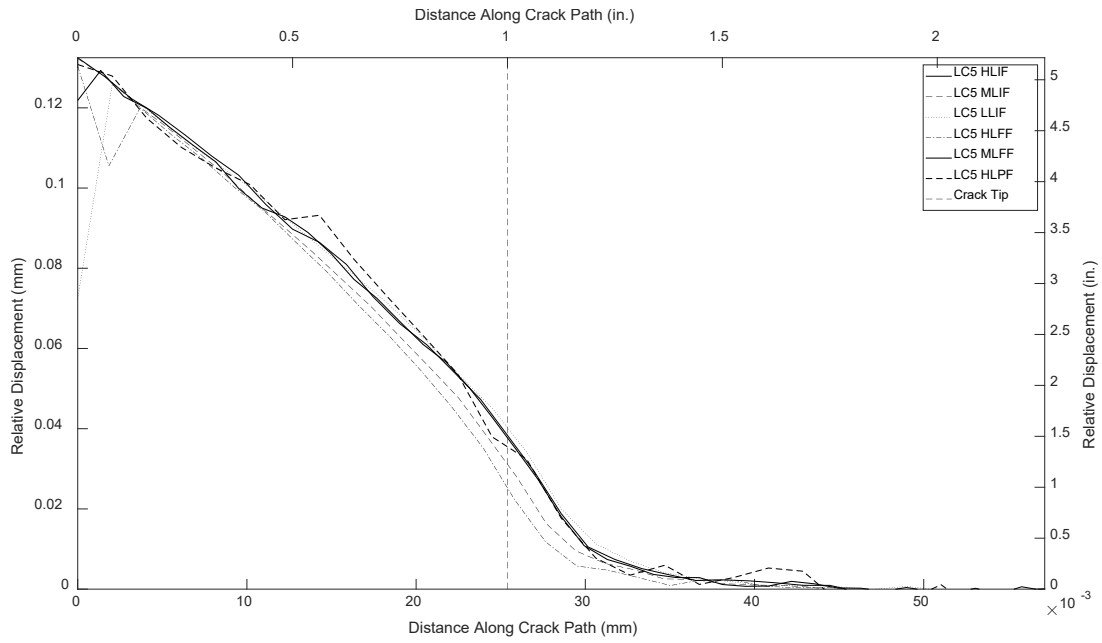
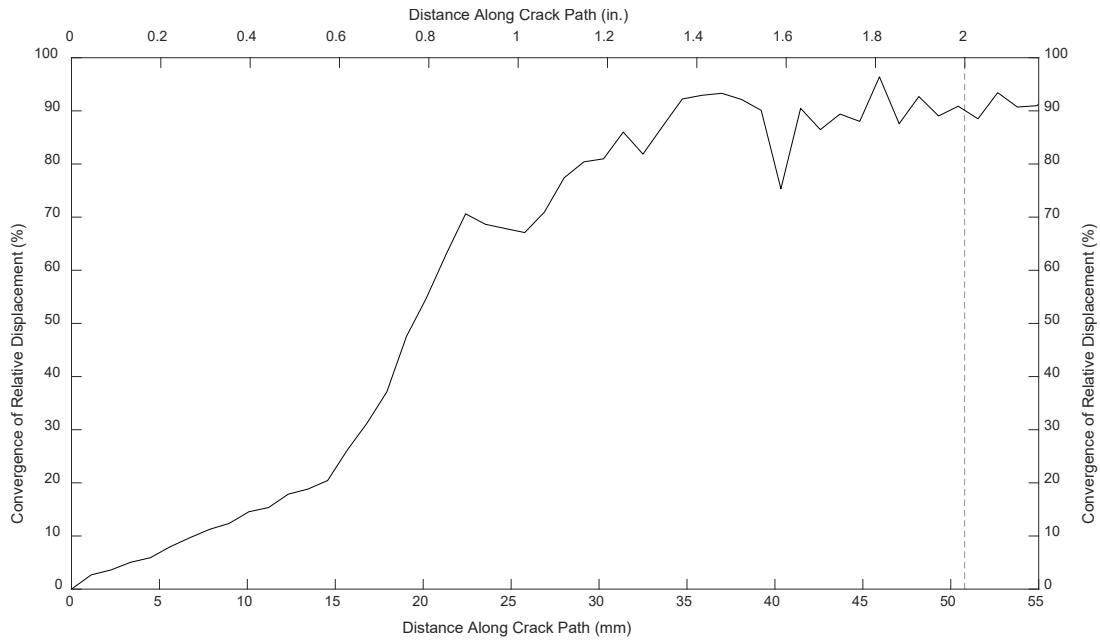Figure A.9 Relative displacement of a 25.4 mm (1.0 in.) crack with a camera distance of 432 mm (17.0 in.) under LC5
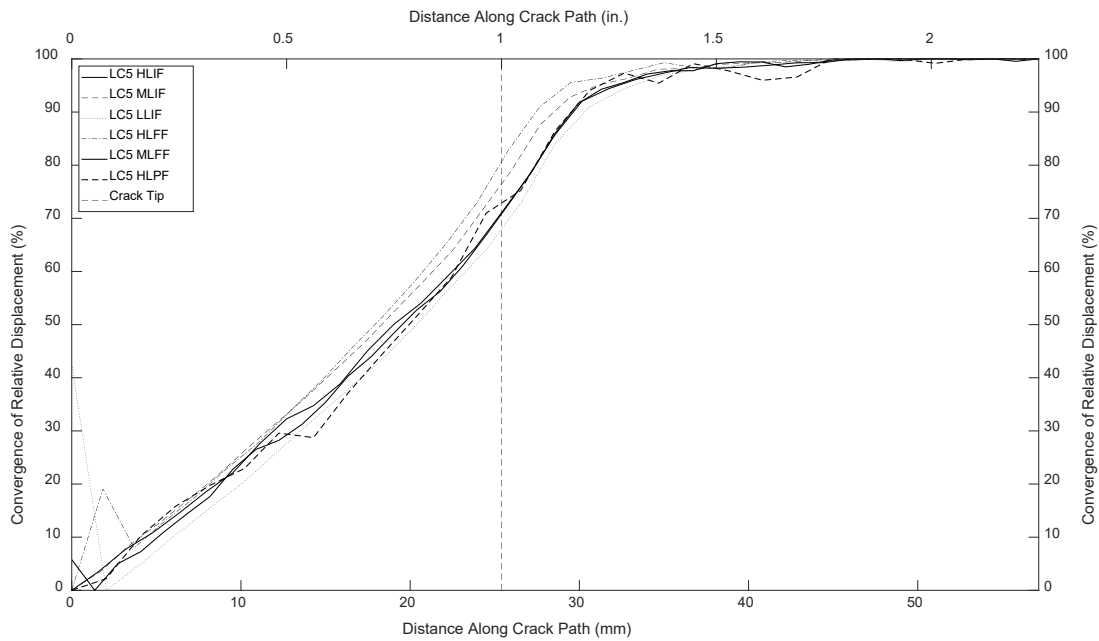
Figure A.10 Convergence of relative displacement of a 25.4 mm (1.0 in.) crack with a camera distance of 432 mm (17.0 in.) under LC5
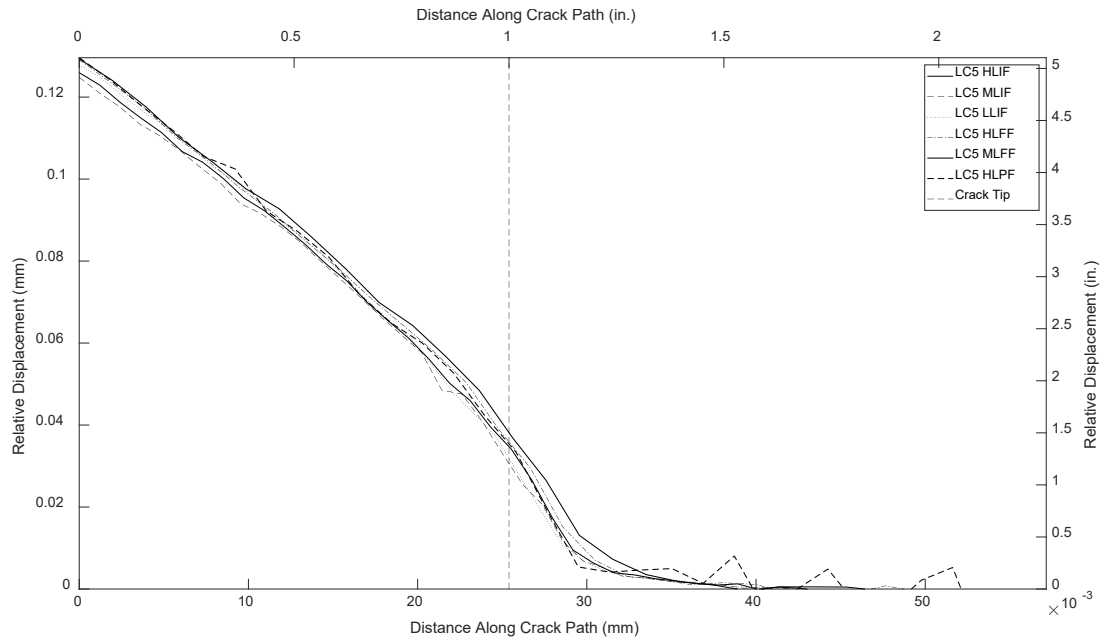
Figure A.11 Relative displacement of a 25.4 mm (1.0 in.) crack with a camera distance of 216 mm (8.5 in.) under LC5
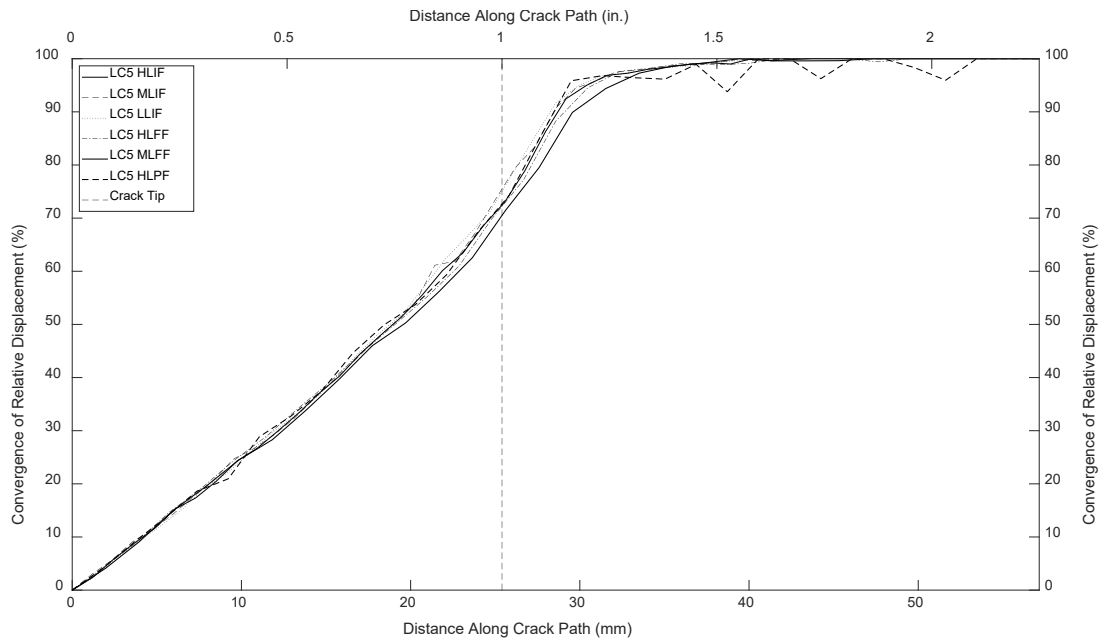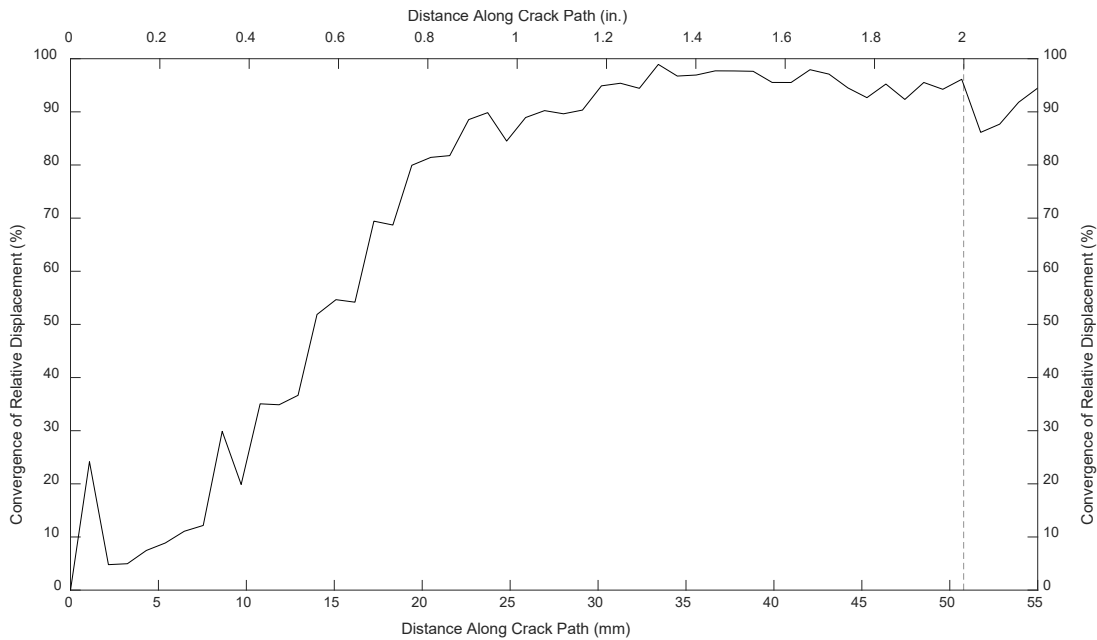

Figure A.12 Convergence of relative displacement of a 25.4 mm (1.0 in.) crack with a camera distance of 216 mm (8.5 in.) under LC5

Convergence values for each condition were averaged across all five load cases for a crack length of 25.4 mm (1.0 in.), shown in tables A.4 through A.6. These tables show a camera-to-specimen distance of 648, 432, and 216 mm (25.5, 17.0, and 8.5 in.), respectively. The convergence for each condition and load case is shown visually in figures A.13 through A.15. These results are representative of each crack length.

Table A.4 Average convergence at 25.4 mm (1.0 in.) crack tip for 648 mm (25.5 in.) camera distance

Light and Focus Condition	Average Convergence	Difference
Ideal	92.6%	N/A
1	71.5%	21.1%
2	72.3%	20.3%
3	69.6%	23.0%
4	73.3%	19.3%
5	66.2%	26.4%
6	73.1%	19.5%

Figure A.13 Average convergence at crack tip for each load case and condition for a 25.4 mm (1.0 in.) crack with a camera distance of 648 mm (25.5 in.)

Table A.5 Average convergence at 25.4 mm (1.0 in.) crack tip for 432 mm (17.0 in.) camera distance

Light and Focus Condition	Average Convergence	Difference
Ideal	92.6%	N/A
1	70.7%	21.9%
2	76.6%	16.0%
3	69.9%	22.7%
4	80.5%	12.1%
5	72.0%	20.6%
6	72.9%	19.7%
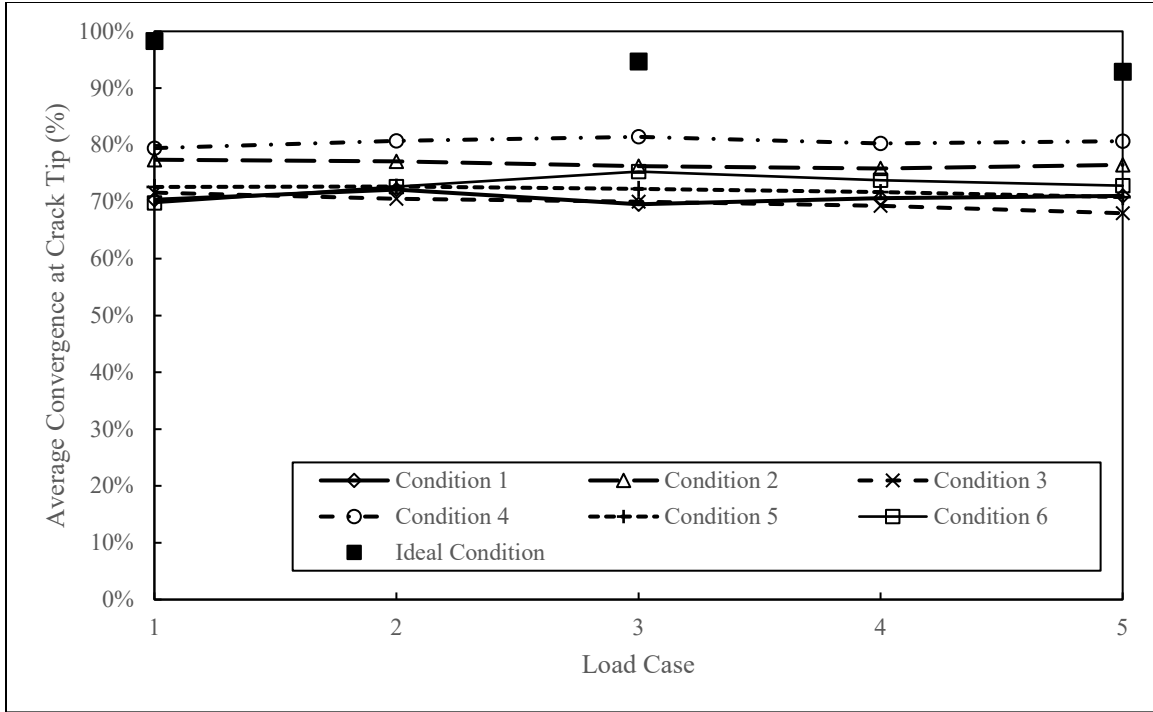
Figure A.14 Average convergence at crack tip for each load case and condition for a 25.4 mm (1.0 in.) crack with a camera distance of 432 mm (17.0 in.)

Table A.6 Average convergence at 25.4 mm (1.0 in.) crack tip for 216 mm (8.5 in.) camera distance

Light and Focus Condition	Average Convergence	Difference
Ideal	92.6%	N/A
1	73.0%	19.6%
2	75.7%	16.9%
3	75.6%	17.0%
4	72.6%	20.0%
5	70.1%	22.5%
6	72.8%	19.8%
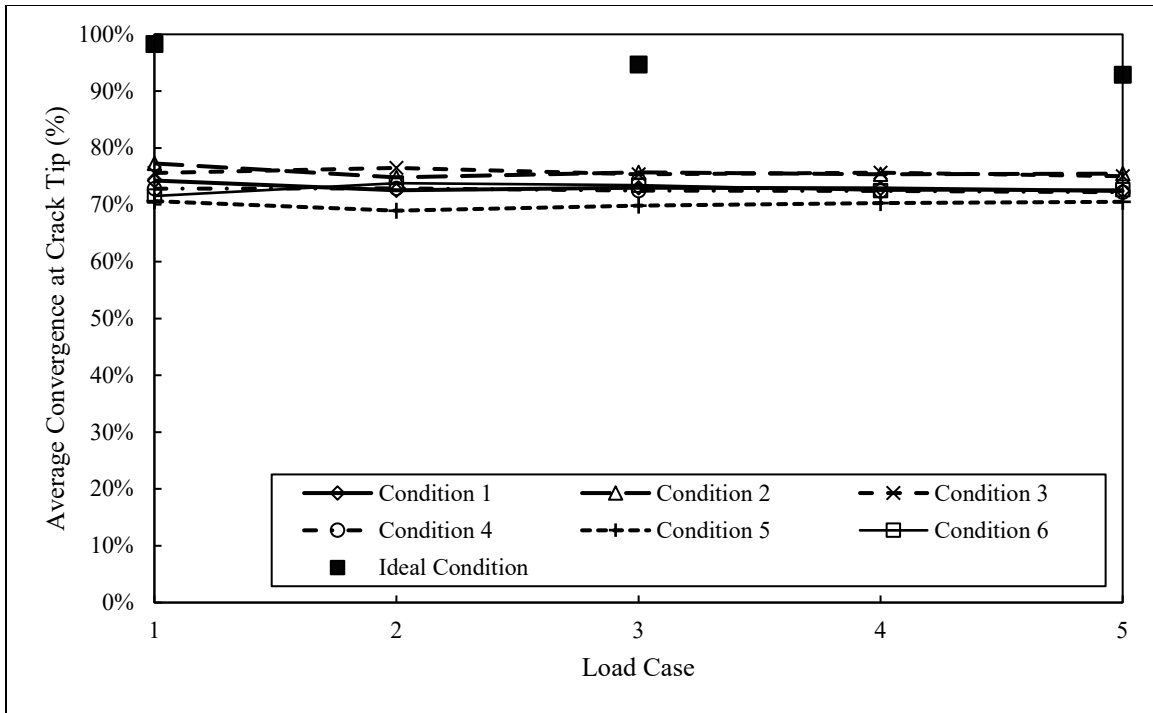
Figure A.15 Average convergence at crack tip for each load case and condition for a 25.4 mm (1.0 in.) crack with a camera distance of 216 mm (8.5 in.)

Figures A.16 through A.23 show the plots of convergence of relative displacement for different aperture values and camera to specimen distances. The vertical dotted line represents the 50.8 mm (2.0 in.) crack length.

Figure A.16 Convergence of relative displacement of a 50.8 mm (2.0 in.) crack with a camera distance of 203.2 mm (8.0 in.) and an aperture of f/1.4 under LC5

Figure A.17 Convergence of relative displacement of a 50.8 mm (2.0 in.) crack with a camera distance of 203.2 mm (8.0 in.) and an aperture of f/2.8 under LC5
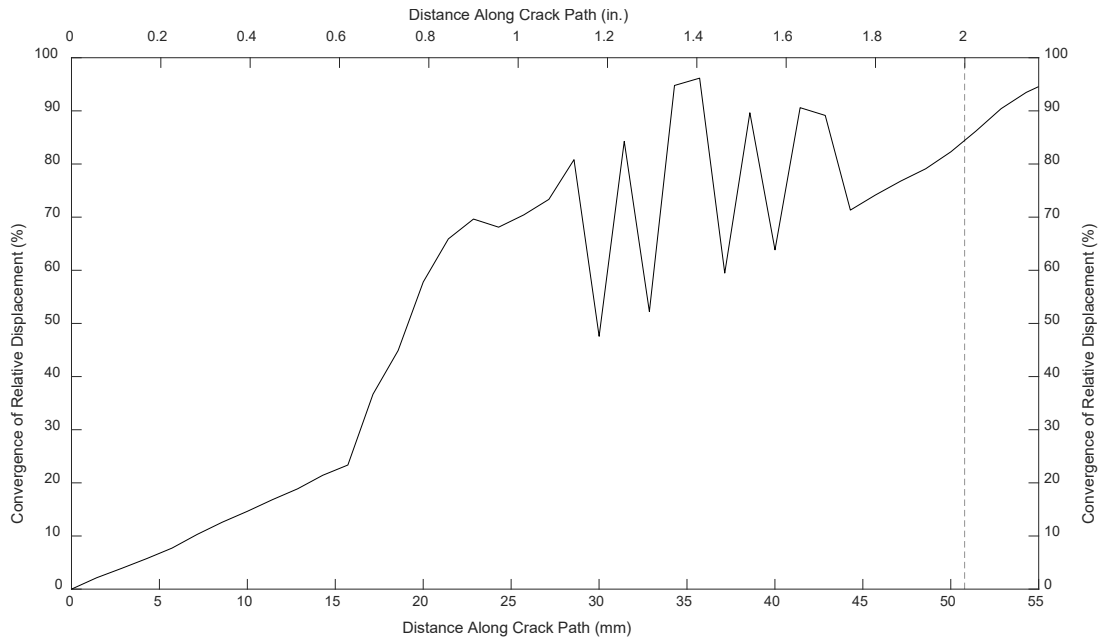
Figure A.18 Convergence of relative displacement of a 50.8 mm (2.0 in.) crack with a camera distance of 304.8 mm (12.0 in.) and an aperture of f/1.4 under LC5
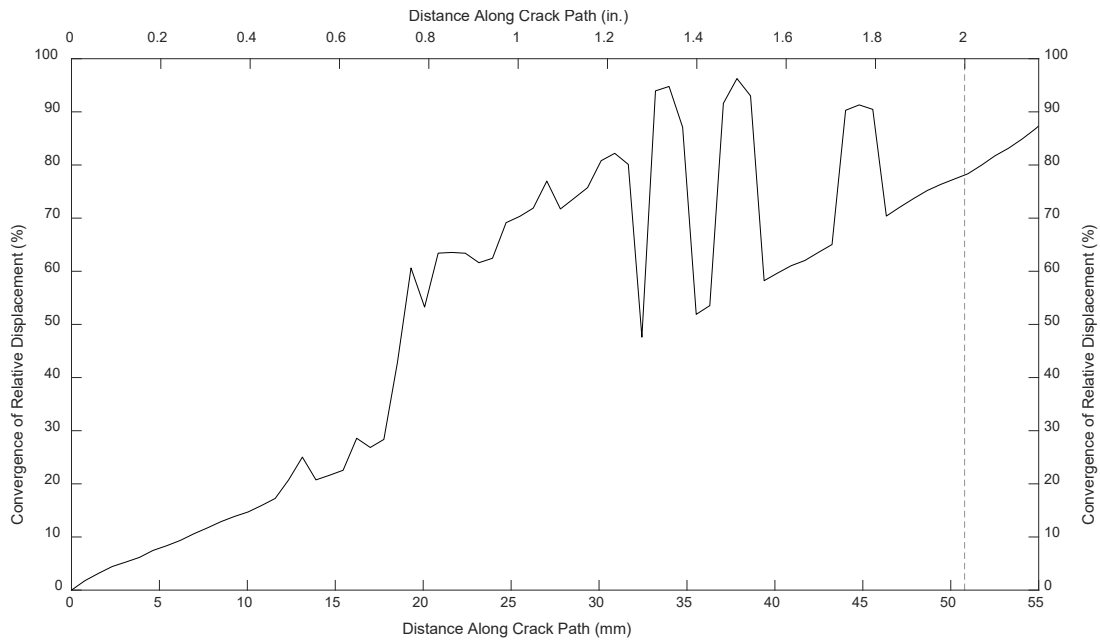
Figure A.19 Convergence of relative displacement of a 50.8 mm (2.0 in.) crack with a camera distance of 304.8 mm (12.0 in.) and an aperture of f/2.8 under LC5
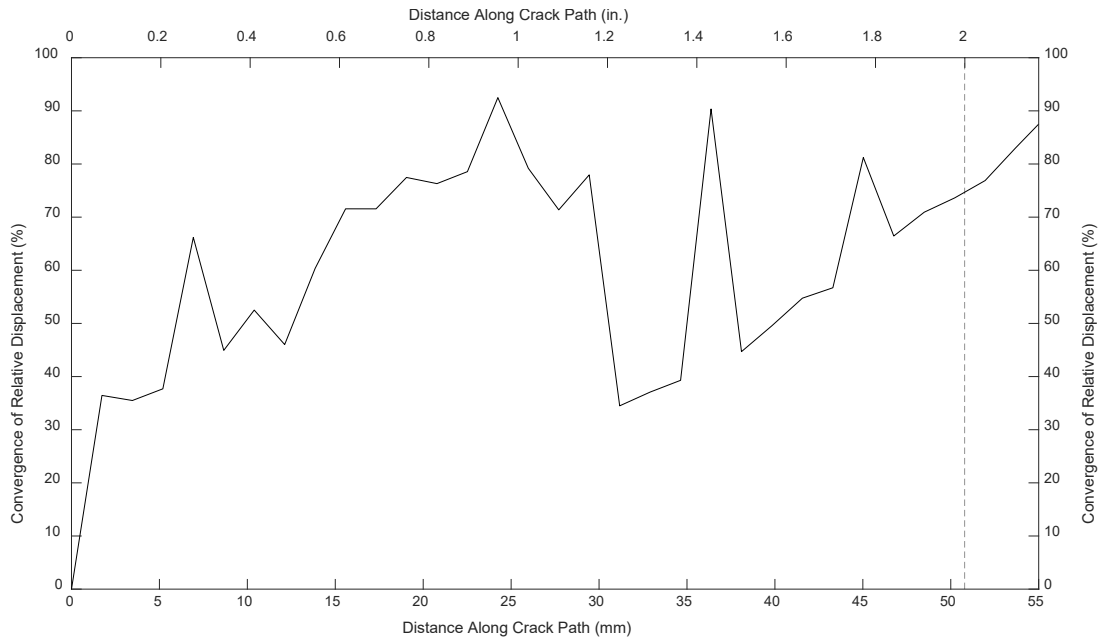
Figure A.20 Convergence of relative displacement of a 50.8 mm (2.0 in.) crack with a camera distance of 457.2 mm (18.0 in.) and an aperture of f/1.4 under LC5
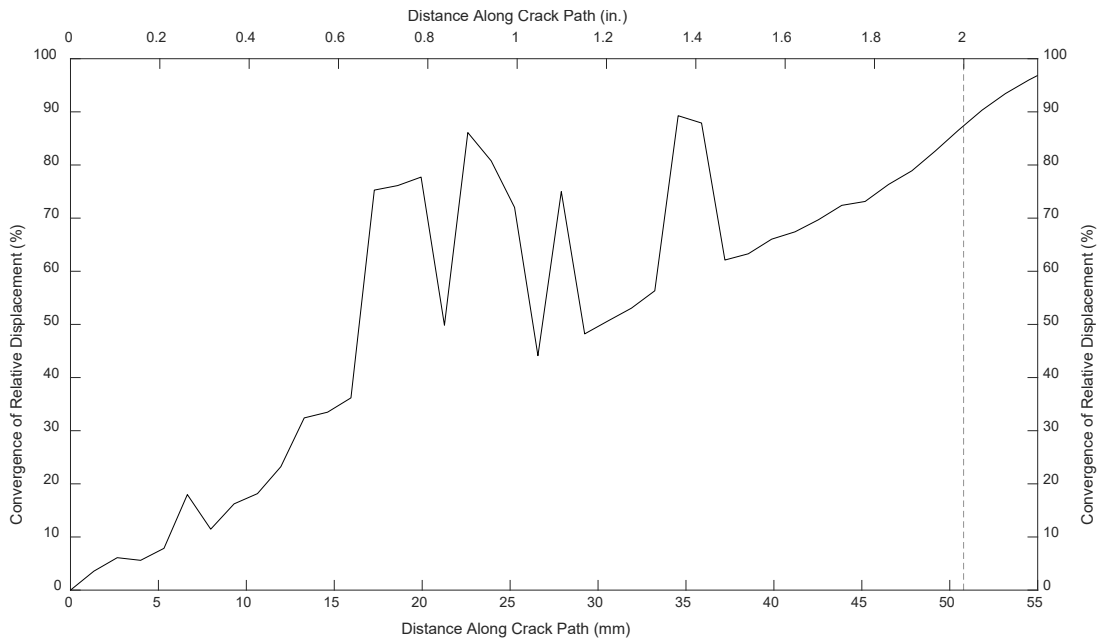
Figure A.21 Convergence of relative displacement of a 50.8 mm (2.0 in.) crack with a camera distance of 457.2 mm (18.0 in.) and an aperture of f/2.8 under LC5
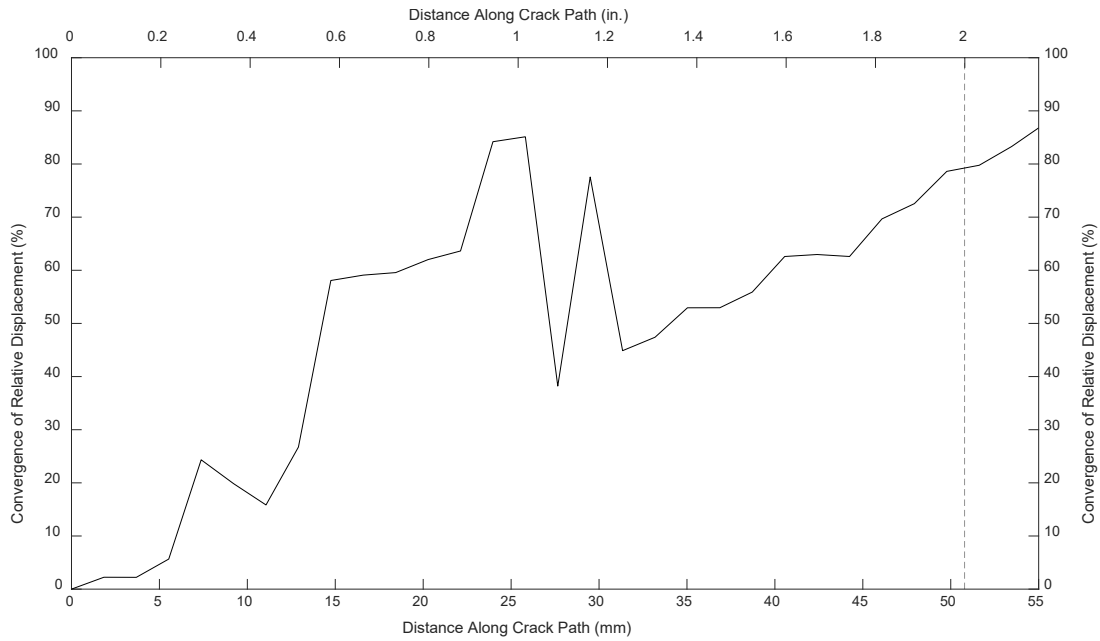
Figure A.22 Convergence of relative displacement of a 50.8 mm (2.0 in.) crack with a camera distance of 609.6 mm (24.0 in.) and an aperture of f/1.4 under LC5
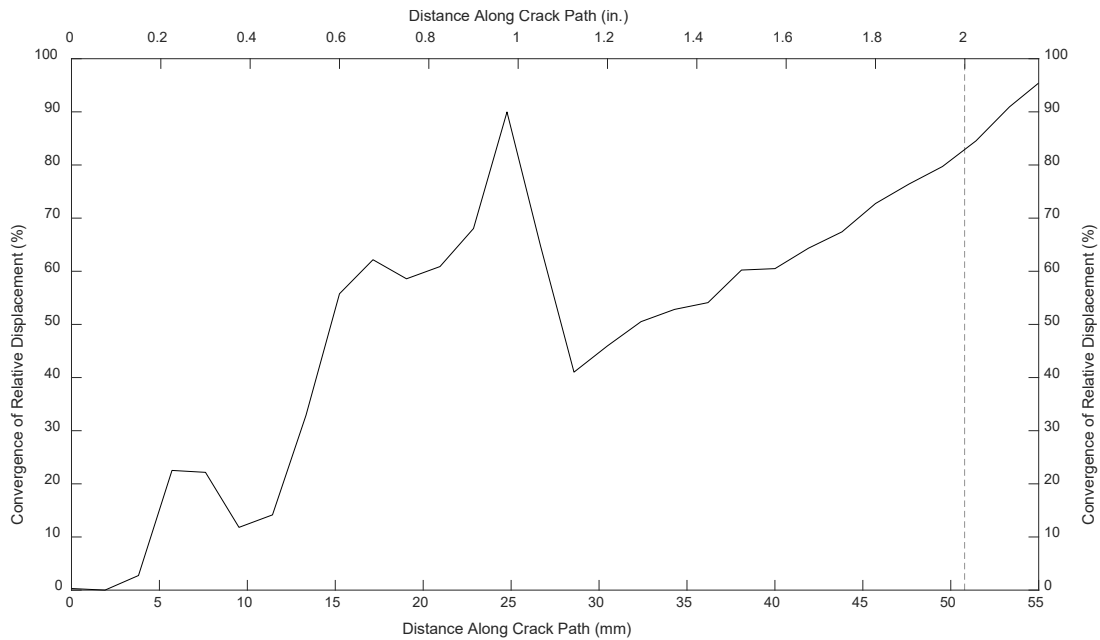
Figure A.23 Convergence of relative displacement of a 50.8 mm (2.0 in.) crack with a camera distance of 609.6 mm (24.0 in.) and an aperture of f/2.8 under LC5

Figures A.24 through A.29 show the in- and out-of-plane crack displacement gradients for the three open-source DIC software packages that were identified as possible alternatives to commercially available DIC. *Ncorr* is shown in figures A.24 and A.25, *ALDIC* is shown in figures A.26 and A.27, and *DICe* is shown in figures A.28 and A.29.
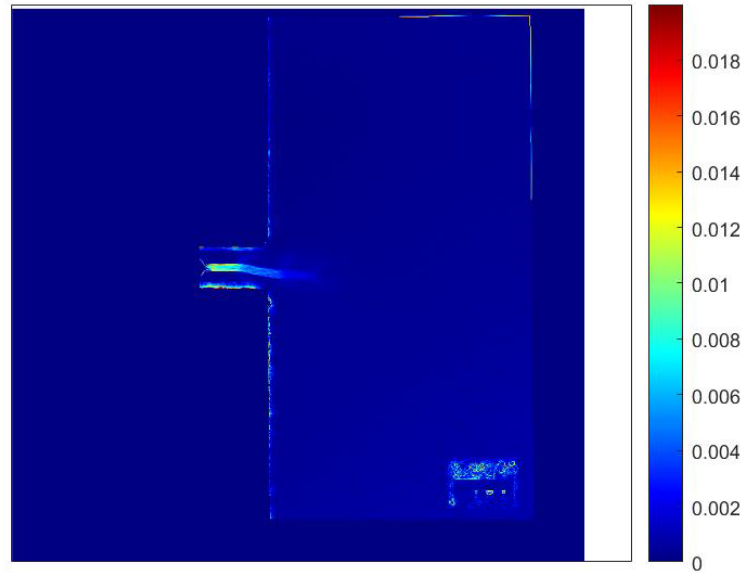
Figure A.24 *Ncorr* in-plane crack displacement gradient
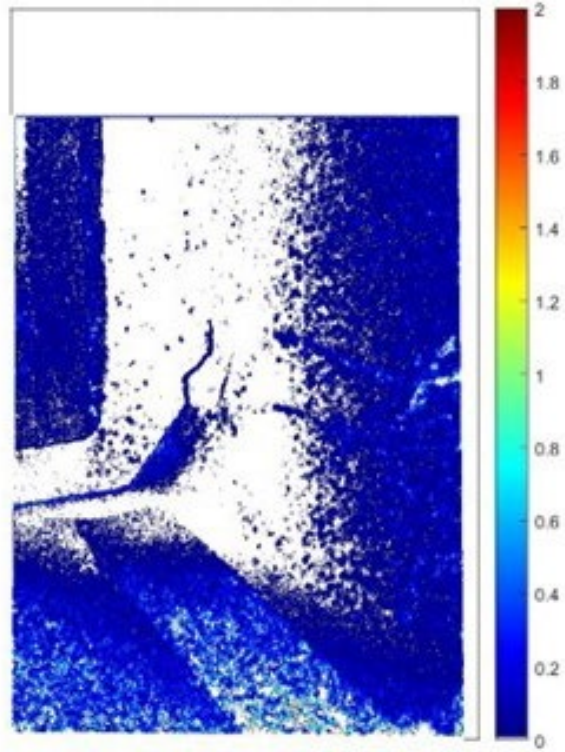
Figure A.25 *Ncorr* out-of-plane crack displacement gradient
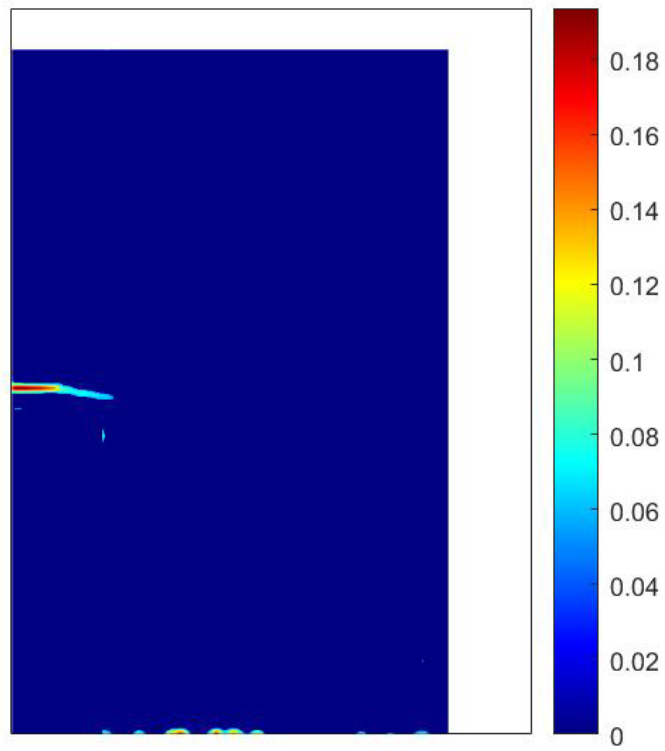
Figure A.26 *ALDIC* in-plane crack displacement gradient
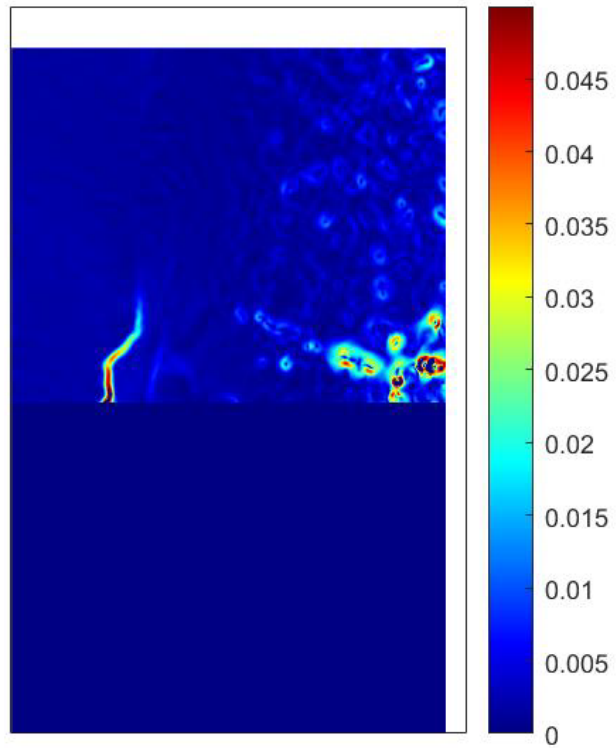
Figure A.27 *ALDIC* out-of-plane crack displacement gradient
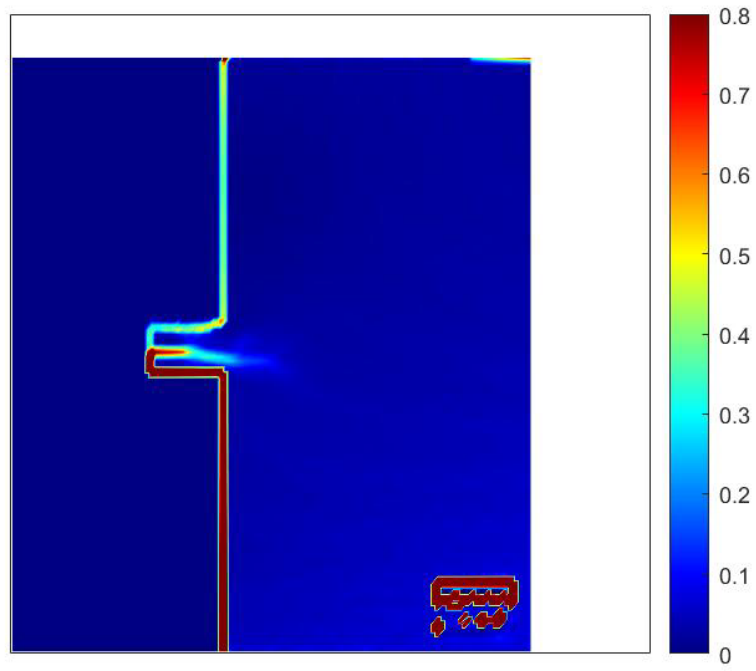
Figure A.28 *DICe* in-plane crack displacement gradient
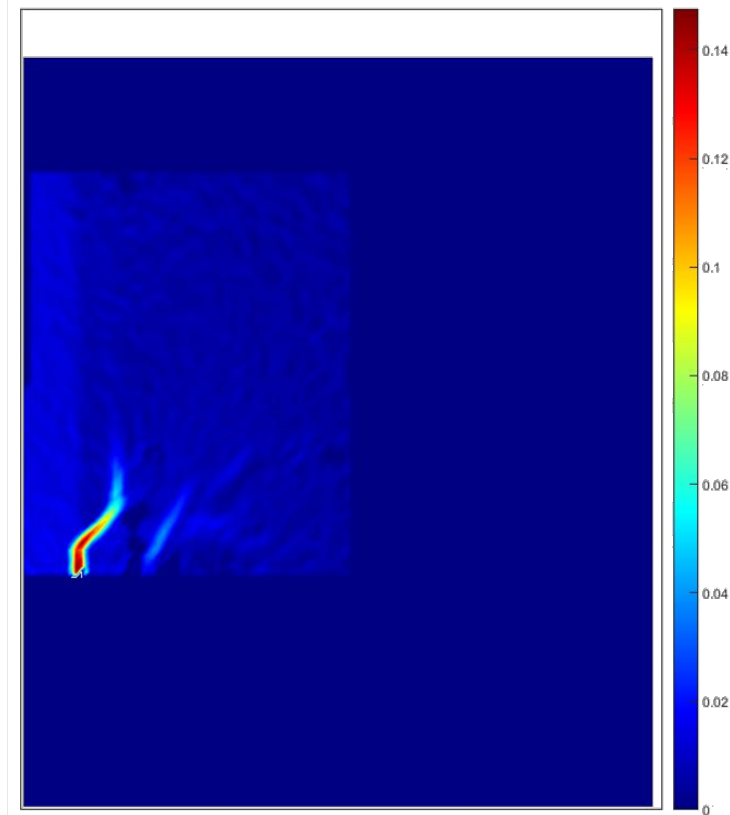
Figure A.29 *DICe* out-of-plane crack displacement gradient

Appendix B Advancements Towards Automation

The plots of convergence of relative displacement for out-of-plane cracking analyzed with a single camera are shown in figures B.1 through B.7. The blue vertical lines represent the different segments of the 44.5 mm (1.75 in.) crack. The red line shows the original data when processed using VIC-3D.
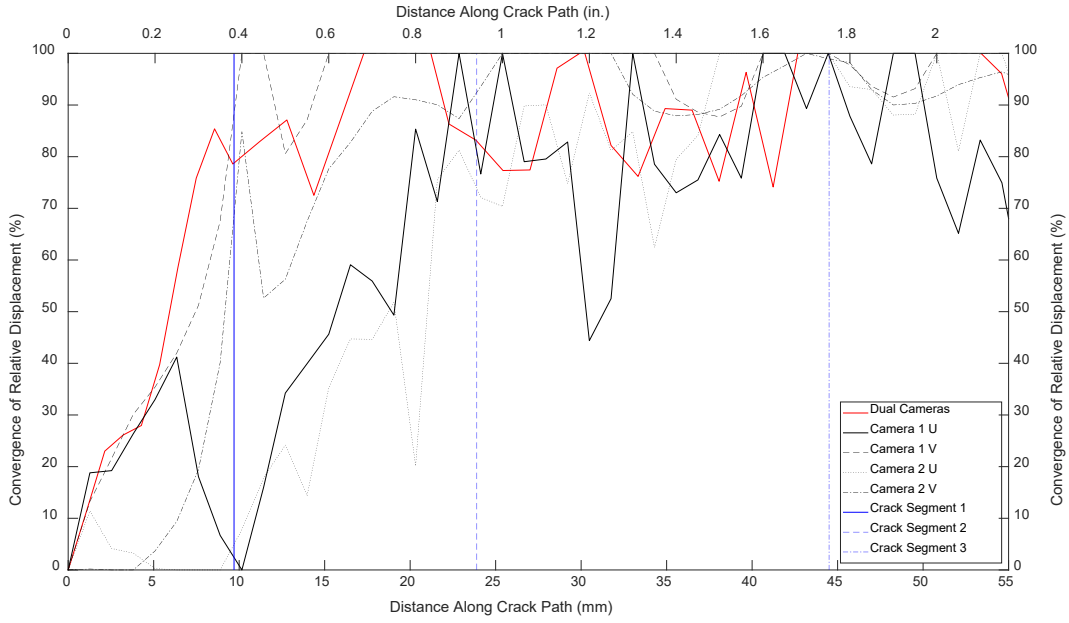
Figure B.1 Convergence of relative displacement of a 44.5 mm (1.75 in.) complex crack under LC1
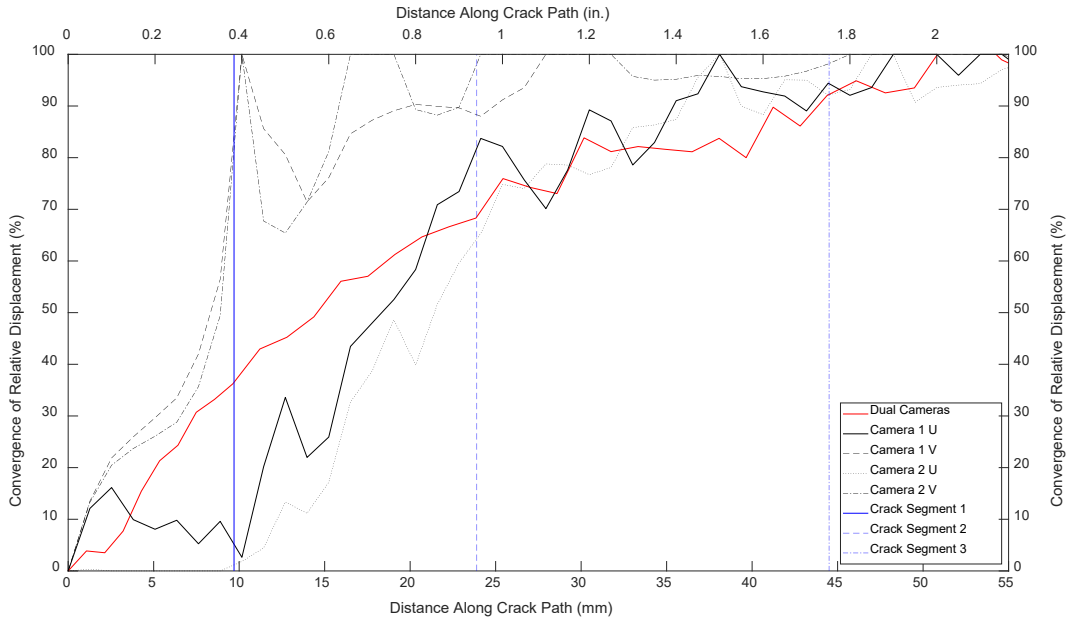
Figure B.2 Convergence of relative displacement of a 44.5 mm (1.75 in.) complex crack under LC2
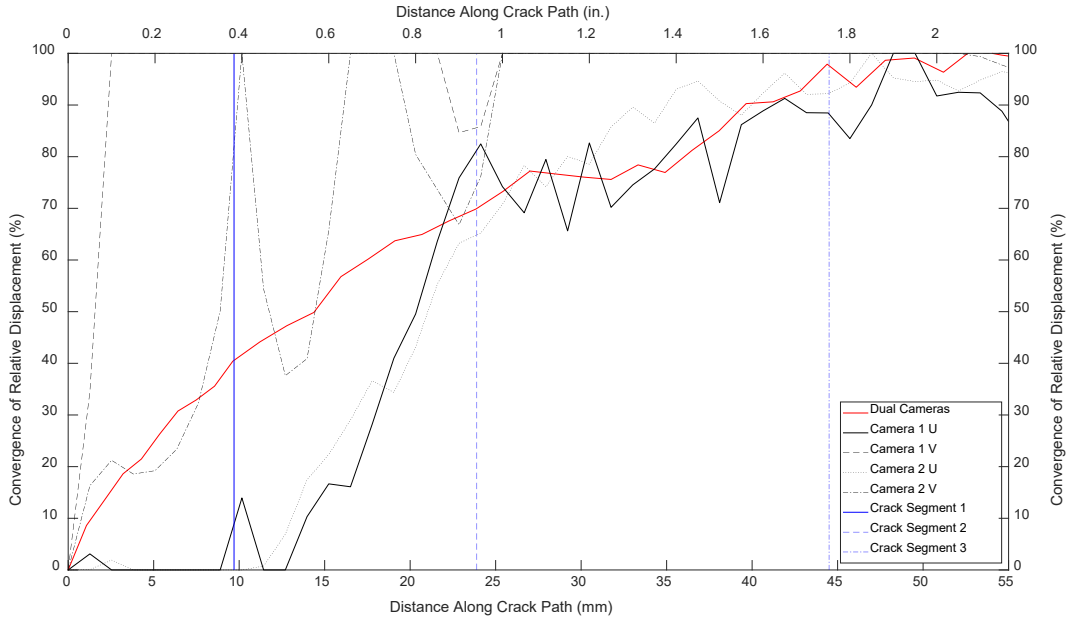
Figure B.3 Convergence of relative displacement of a 44.5 mm (1.75 in.) complex crack under LC3
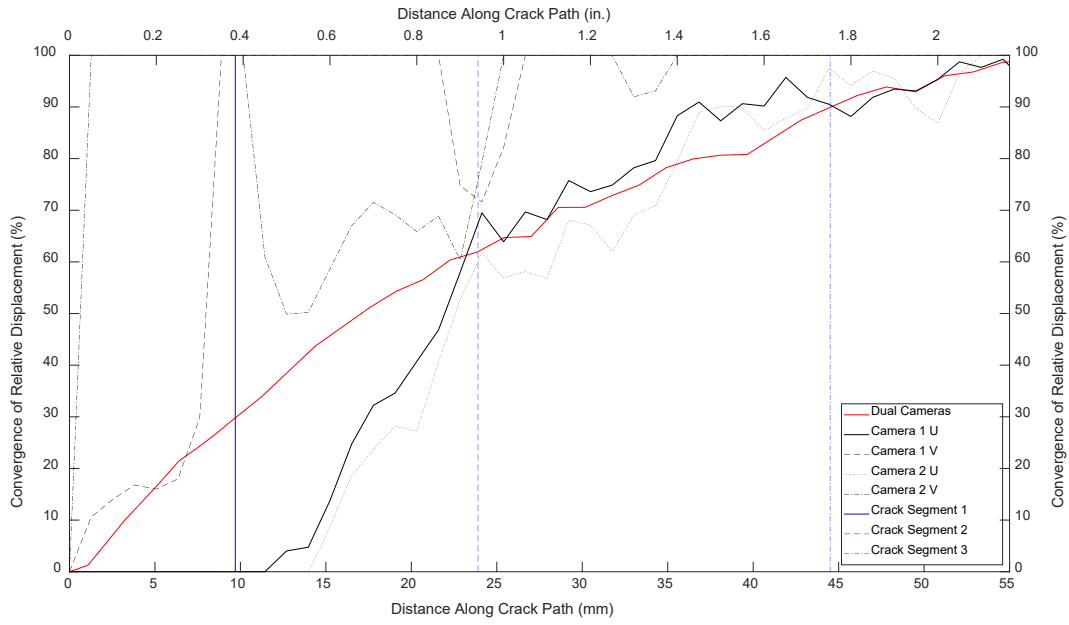

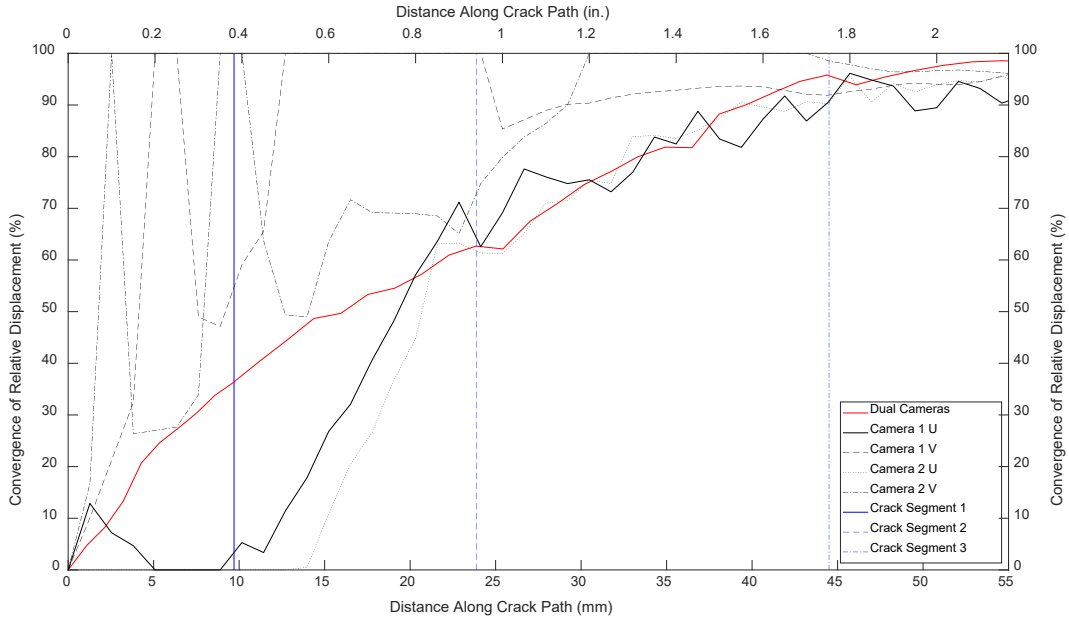Figure B.4 Convergence of relative displacement of a 44.5 mm (1.75 in.) complex crack under LC4

Figure B.5 Convergence of relative displacement of a 44.5 mm (1.75 in.) complex crack under LC5
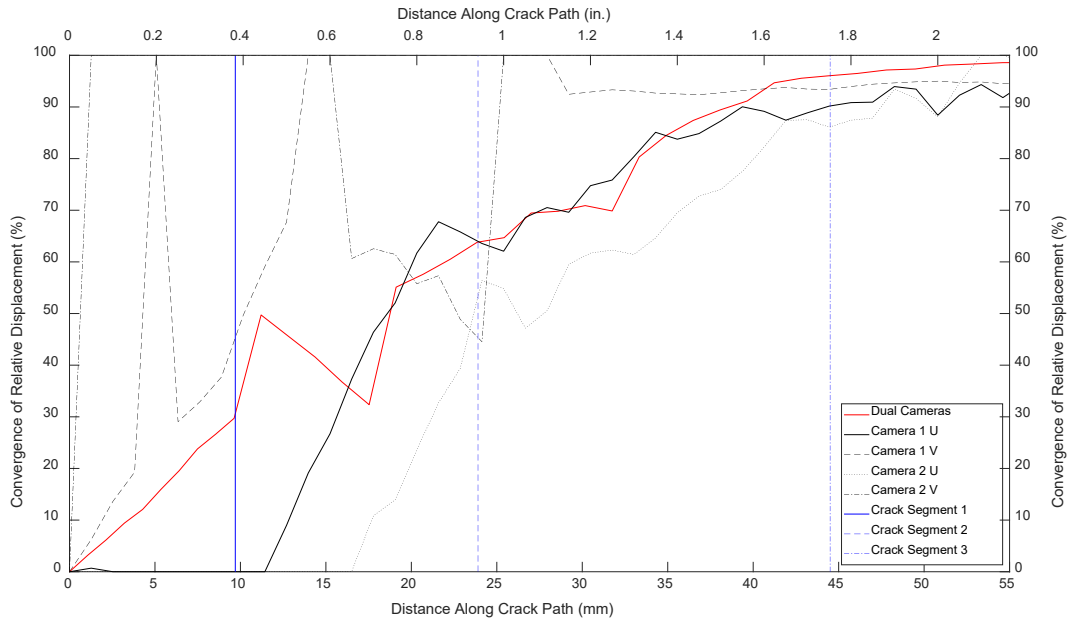

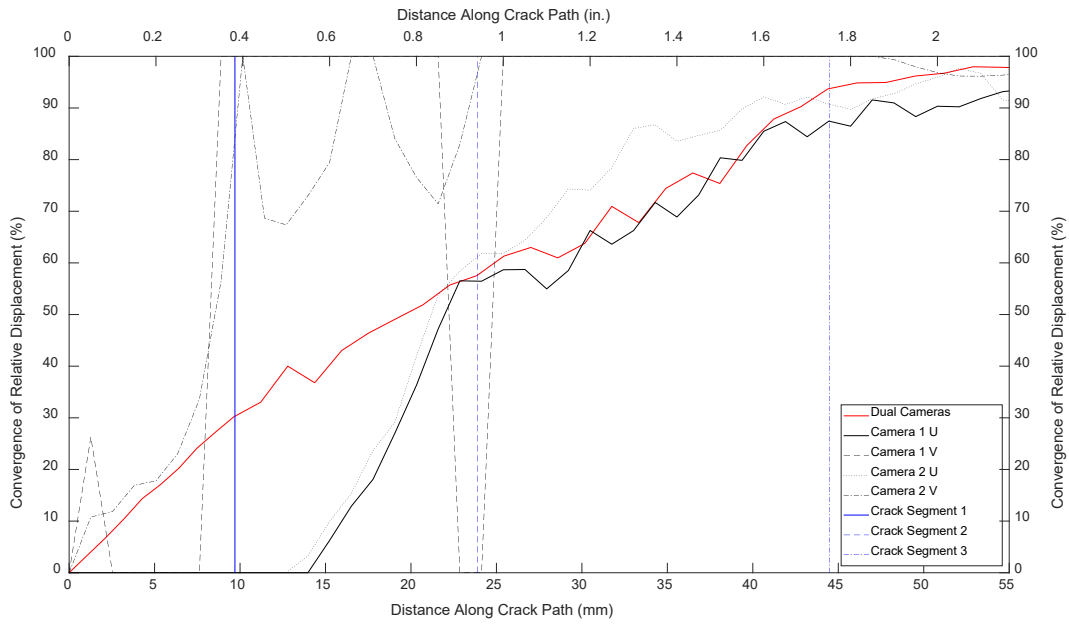Figure B.6 Convergence of relative displacement of a 44.5 mm (1.75 in.) complex crack under LC6

Figure B.7 Convergence of relative displacement of a 44.5 mm (1.75 in.) complex crack under LC7